Wave effect mechanisms enhancing air–sea CO_2 exchange and modulating seawater carbonate–pH adaptation in the POP2–waves coupled model

Yung-Yao Lan[1,2], Huang-Hsiung Hsu[1], Wei-Liang Lee[*1] and Simon Chou[1]

[1]Research Center for Environmental Changes, Academia Sinica, Taipei 11529, Taiwan

[2]National Land Resources Conservation Center, National Chung Hsing University, Taichung 40227, Taiwan

Correspondence to: Wei-Liang Lee (leelupin@gate.sinica.edu.tw)

Abstract

Wave and bubble-mediated processes impact air–sea CO_2 flux by enhancing the gas transfer velocity—normalized to a Schmidt number of 660 ($K_{w,660}$)—primarily through their dependence on significant wave height (H_s). Neglecting wave and bubble processes may lead to an underestimation of air–sea CO_2 flux under high 10-m wind speeds (U_{10}) in most state-of-the-art climate models. In this study, a waves module from the Princeton Ocean Model (POM) is integrated into the Parallel Ocean Program version 2 (POP2) within the CESM1.2.2 framework. This coupled model, termed POP2–waves, is evaluated alongside a control simulation (B–CTL) against National Oceanic and Atmospheric Administration (NOAA) CarbonTracker (CT2022) air–sea CO_2 flux data. Overall, bubbles contribute up to 41.3% to the total air–sea CO_2 flux, a finding consistent with recent literature. Furthermore, the spatial distribution of air–sea CO_2 flux in POP2–waves broadly agrees with NOAA CT2022 product, although regional discrepancies remain. Under the $dpCO_2$-driven negative feedback, the POP2–waves experiment yields increases of 11.8% and 41.6% in negative and positive air–sea CO_2 flux regions, with a 1.8% increase in the global ocean carbon sink compared to the B–CTL control. The air–sea $dpCO_2$ (pH) exhibits the strongest positive (negative) regression coefficient with air–sea CO_2 flux across the global ocean. Additionally, $K_{w,660}$ shows a positive (negative) regression coefficient with the positive (negative) air–sea CO_2 flux regions, while SST displays the opposite pattern relative to $K_{w,660}$.

1. Introduction

The exchange of CO_2 between the air and sea is a crucial component of the global carbon cycle, carrying significant implications for Earth's climate (Bange et al., 2024; Friedlingstein et al., 2022; McKinley et al., 2020; Müller et al., 2023; Shutler et al., 2019). Traditionally, the exchange of CO_2 across the air–sea interface can be characterized using the following bulk formula (e.g., Wanninkhof, 1992, 2014; McKinley et al., 2020; Dong et al., 2022; Fay et al., 2021; Zhou et al., 2023; Heimdal et al., 2024):

$$FCO_2 = K_{w,660} \cdot k_0 \cdot (pCO_2^w - pCO_2^a) \cdot (1 - ice) \quad (1)$$

where the air–sea CO_2 flux (FCO_2) is determined by the gas transfer velocity expressed relative to a Schmidt number of 660 ($K_{w,660}$), the difference in partial pressure of CO_2 ($dpCO_2$) between the seawater and atmosphere (indicated by superscripts " *w* " and " *a* ", respectively), and the solubility constant (k_0), which varies with salinity and temperature (Weiss, 1974). The direction of positive or negative air–sea CO_2 flux follows $pCO_2^w - pCO_2^a$, with positive air–sea CO_2 flux indicating ocean outgassing to the atmosphere. Moreover, the fluxes are weighted by 1 minus the ice fraction (*ice*). The estimation of bulk air–sea CO_2 fluxes in $K_{w,660}$ is typically similar to the Wanninkhof (1992) equation:

$$K_{w,660} = 0.31 \langle U_{10}^2 \rangle (Sc/660)^{-0.5} \quad (2)$$

where $\langle U_{10}^2 \rangle$ represents the squared neutral mean wind speed at 10 m above the surface, and *Sc* denotes the Schmidt number. The flux estimate error can reach as high as 34% due to model limitations and uncertainties surrounding bulk parameters. (Signorini and McClain, 2009). However, significant uncertainties persist in estimates of air–sea CO_2 flux, primarily stemming from an incomplete understanding of the spatiotemporal variability in the governing mechanisms (Shutler et al., 2019).

Some studies have highlighted that estimating air–sea CO_2 fluxes involves

considerations beyond just neutral wind speed and solubility factors. Monahan and Spillane (1984) previously regarded whitecaps as "low impedance vents", effectively "shortening" the water-side transfer resistance. Without wave breaking, air–sea CO_2 exchange occurs via mass transport, which under non-turbulent conditions is governed by molecular diffusion, while breaking acts as a transitional process from laminar to turbulent flow (Deike, 2022). Bubbles offer an extra surface for gas transfer, rising through the water-side mass boundary layer of the water surface and bursting at the water surface, enhancing near-surface turbulence (Soloviev and Lukas, 2010; Bell et al., 2017; Deike and Melville, 2018; Krall et al., 2019; Czerski et al., 2022). Gutiérrez-Loza et al. (2022) pointed out that sea spray transported into the atmosphere and ultimately evaporating serves an efficient mechanism for air–sea CO_2 exchange during high and intermediate wind speeds (above 6–8 m s^{-1}), whereas during low wind speeds (<6 m s^{-1}), water-side convection was identified as a significant control mechanism. Several studies corroborate the significance of breaking waves and bubble injection mechanisms in facilitating CO_2 transfer (e.g., Andreas et al., 2016; Brumer et al., 2017; Blomquist et al., 2017; Reichl and Deike, 2020; Li et al., 2023; Zhou et al., 2023; Rustogi et al., 2025). Deike and Melville (2018) demonstrated that the bubble-mediated contribution to CO_2 transfer exceeds 40% at a neutral 10-meter wind speed (U_{10}) is ≥ 10 m s^{-1}, becoming dominant at $U_{10} \geq 15$ m s^{-1} and reaching 60% at 20 m s^{-1}.

Monitoring the sea surface CO_2 content is crucial for comprehending the Earth system, as climate change has begun to impact the ocean's carbon uptake capacity (Behncke et al., 2024). However, indirect estimates of partial pressure of CO_2 (pCO_2) derived from pH and salinity measurements still entail uncertainties (e.g., Williams et al., 2017; Gray et al., 2018; Coggins et al., 2023; Behncke et al., 2024; Fay et al., 2024; Yang et al., 2024). Direct flux measurements in marine environments using the eddy covariance method can be conducted with both open- and closed-path analyzers. A

closed-path infrared gas analyzer (e.g., LI-7000, LI-COR) operates with an enclosed measurement chamber (Sutton et al., 2014, 2021; Bakker et al., 2016; Sabine et al., 2020; Akhand et al., 2021; Wu and Qi, 2023), whereas open-path analyzers (e.g., LI-7500, LI-COR) measure infrared absorption directly in ambient air (Edson et al., 2011; Tokoro et al., 2014; Bell et al., 2017; Dong et al., 2021; Van Dam et al., 2021). Both types are affected by H_2O cross-sensitivity, but each has its own advantages and limitations (Honkanen et al., 2018). Local air–sea CO_2 flux observations present challenges for validating global Earth system models (ESMs) because direct long-term global observations of air–sea CO_2 flux are limited. As a result, most validation datasets are derived from sparse ship-based pCO_2 observations combined with statistical interpolation, machine learning, atmospheric inversion, and climatological averaging to construct gridded long-term flux products.

Several recent studies have estimated the air–sea CO_2 flux using Eq. (1), while current parameterizations in oceanic and atmospheric models still rely exclusively on neutral wind speed (Long et al., 2013; Moore et al., 2013; Couldrey et al., 2016; Jin et al., 2017; Lovenduski et al., 2019; Ziehn et al., 2020; Chikamoto and DiNezio, 2021) and through surface ocean observation-based products, with air–sea CO_2 flux calculated using a bulk parameterization approach (Wanninkhof et al., 1992, 2014; Fay et al., 2021). The uptake of anthropogenic CO_2 by the oceans is lowering pH and altering carbonate chemistry in nonlinear ways, further reducing the oceans' capacity to absorb additional CO_2 (Moore et al., 2013). The mechanisms of breaking waves and bubble injection in facilitating $K_{w,660}$ have been examined primarily through data analysis of non-model simulations (e.g., Andreas et al., 2016; Blomquist et al., 2017; Reichl and Deike, 2020; Zhou et al., 2023). Rustogi et al. (2025) employs a fully coupled ocean–biogeochemistry modeling system based on the MOM6 ocean circulation model and the COBALTv2 biogeochemical module. This framework simulates ocean dynamics,

temperature, and carbon cycling processes including dissolved inorganic carbon (DIC), pCO_2, and wave effects in the air–sea CO_2 exchange. They also describe a nonlinear pCO_2 feedback mechanism within the coupled ocean–carbon system that regulates air–sea CO_2 flux.

In this study, we aim to investigate the significance of breaking waves and bubble injection mechanisms through ocean biogeochemistry response on the air–sea CO_2 flux and ocean's buffering capacity through the carbonate–pH system, using the Parallel Ocean Program version 2 (POP2; Smith et al., 2010) of the Community Earth System Model version 1.2.2 (CESM1.2.2; Hurrell et al., 2013) coupled with waves module (Mellor et al., 2008) of the Princeton Ocean Model (POM; Blumberg and Mellor, 1987). The coupled model is referred to as POP2–waves.

The structure of this paper is organized as follows. Section 2 introduces the model, data, methodology, and experiments employed in this study. Twelve key regions of high air–sea CO_2 flux variability, identified by NOAA CT2022, are defined here to validate the model-simulated air–sea CO_2 fluxes. The performance of the POP2–waves coupled model in simulating air–sea CO_2 flux and its interaction with the carbonate–pH system over the Western Pacific region (WP, 160–180°E, 35–40°N) and the Equatorial Pacific region (EP, 230–250°E, 0–5°S) in Section 3, while Section 4, we compare the carbonate–pH dynamics of POP2–waves and B–CTL, examine the primary drivers of air–sea CO_2 exchange, and evaluate the uncertainties arising from the absence of $dpCO_2$-driven negative feedback. Finally, Section 5 presents the conclusions.

2. Data, model experiments, and methodology

2.1 Description of the model framework and experiments

In this study, we investigated the role of waves and bubble mechanisms through ocean biogeochemistry response between B–CTL and POP2–waves coupled model in

CESM1.2.2 framework (Fig. 1). The CESM simulation is conducted using a fully coupled component set over a 30-year period, with well-mixed greenhouse gases (CO_2, CH_4, N_2O, etc.), ozone, and aerosols fixed to year-2000 values (B_2000_CAM5 compsets). It has a horizontal resolution of 1.9° × 2.5° in Community Atmosphere Model 5.3 (CAM5.3) and a nominal 1° horizontal resolution with 60 vertical layers in POP2, Community Land Model version 4 (CLM4), prognostic Los Alamos Sea Ice Model (CICE), and the coupler (CPL) (Hurrell et al., 2013). POP2 is forced by the atmosphere (CAM5.3) through the coupler (CPL), including (1) momentum fluxes (zonal and meridional wind stress and friction velocity), (2) heat fluxes (net shortwave radiation, sensible heat flux, longwave radiation, and heat flux from snow and ice melt), (3) freshwater fluxes (precipitation, evaporation, river runoff, and ice melt), and (4) surface winds (10 m zonal and meridional wind speeds). POP2 interacts with the Marine Biogeochemistry (MARBL; Long et al., 2021) module via ocean dynamics (currents and sea surface height), K-profile vertical mixing, and tracer transport, with additional contributions from the wave module, to influence carbonate chemistry and air–sea CO_2 flux. In the MARBL module, changes in DIC and nutrients (NO_3, PO_4, and Fe) are primarily controlled by biological processes. Photosynthesis consumes DIC and nutrients, while respiration and remineralization return carbon to DIC. Together with the wave module, these processes regulate the carbon cycle and influence air–sea CO_2 exchange. This study follows the NCAR CESM1 framework, in which the default friction velocity (u^*) is computed in the CPL as part of the bulk aerodynamic formulation for air–sea momentum exchange.

A control air–sea CO_2 flux and seawater acidification simulation (B–CTL) uses Eq. (1), where $K_{w,660}$ is the Wanninkhof (1992) equation (Eq. 2). We use the present-day scenario (starting from the year 2000) to estimate air–sea CO_2 flux, $pCO_2^w - pCO_2^a$ and pH across both B–CTL and POP2–waves experiments, allowing us to focus on the

impact of wave effects on carbonate chemistry and to compare the results with the existing NOAA CT2022 (Jacobson et al., 2023). In the wave effect mechanism simulations, we coupled the waves module (Mellor et al., 2008) of the POM model into POP2 (POP2–waves experiment) and incorporated bubble-mediated gas transfer, computed from a mechanistic model for air bubble entrainment at the breaking wave scale (Deike and Melville, 2018), combined with the POP2 biogeochemistry response.

POP2–waves experiment adopts the parameterization proposed by Deike and Melville (2018), Reichl and Deike (2020), and Deike (2022) for both the non-bubble-mediated and bubble-mediated gas transfer velocity as a function of friction velocity, u_* (m s^{-1}) and significant wave height, H_s (m). This parameterization captures the main wave effect, as well as solubility and diffusivity, effectively consolidating for CO_2 by expressing relative to a Schmidt number of 660 for the gas transfer velocity as the sum of the non-bubble ($k_{wNB,660}$) and bubble ($k_{wB,660}$) components, following Deike and Melville (2018):

$$K_{w,660} = K_{wNB,660} + K_{wB,660} = A_{NB} u_* \left(\frac{Sc}{660}\right)^{-1/2} + \frac{A_B}{K_0 R T_0} u_*^{5/3} (g H_s)^{2/3} \left(\frac{Sc}{660}\right)^{-1/2} \quad (3)$$

where A_{NB} is an empirical, nondimensional coefficient given as 1.55 ×10^{-4}, A_B is a dimensional fitting coefficient (1.2 ×10^{-5} s^2 m^{-2}), R is the ideal gas constant (0.082 L atm mol^{-1} K^{-1}), T_0 is the sea surface temperature, SST (K), and g is gravitational acceleration (9.806 m s^{-1}). In addition, Section 3.3 will examine the contribution ratios of the non-bubble and bubble components in simulating the air–sea CO_2 flux.

2.2 Coupling POP2–waves Methodology

The architecture for the POP2–waves experiment in the CESM1.2.2 framework is shown in Fig. 1. Except for the ocean component, all other components follow the CESM 1.2.2 framework. The wave module requires variables to be passed through the

CPL, POP2, and an input file. In addition to the original component relationships in CESM1.2.2, we obtain zonal and meridional 10-m winds, as well as friction velocity (including sea surface and the ice fraction) from the CPL to calculate the wave's property and $K_{w,660}$. We require physical variables from POP2 to drive the wave module calculations, including interpolating the depth-variable currents of the POP2 z-coordinates (60 levels of zonal and meridional horizontal velocity) into the POM (waves) sigma-coordinates (21 levels) for calculating the depth-dependent wave radiation equation and the specified spectrum, as well as ocean grid information in the x, y, and z coordinates and the timestep information. The wave module requires external input variables (F1–F4), which are spectrally averaged components of wave radiation stress used in the momentum equation.

When simulating wave energy or propagation, ignoring parallel computational efficiency can cause artificial wave energy buildup at block boundaries in the domain decomposition. This study follows the POP2 Message Passing Interface (MPI) protocol for parallel computing, incorporating wave-module variables such as zonal and meridional 10-m winds, wave radiation stress, subsurface momentum, and wave radiation and energy densities, as illustrated by the blue circle in Fig. 1.

2.3 Model Validation

We compare the spatial patterns of air–sea CO_2 flux simulated by the control CESM1 simulation (B–CTL) and the POP2–waves model against estimates from the NOAA CarbonTracker data assimilation system (CT2022; Jacobson et al., 2023). Unlike our ocean-centric simulations, CT2022 adopts an atmospheric perspective, inferring air–sea CO_2 fluxes from observed atmospheric CO_2 mole fractions. This product integrates the cumulative effects of anthropogenic and natural carbon processes to provide global flux estimates from January 2000 to December 2020.

Adopting the framework established by Jacobson et al. (2007), NOAA CT2022 partitions the global ocean into 30 basins to accurately represent large-scale circulation and biogeochemical dynamics. This basin-based approach groups regions by their internal coherence in physical processes—such as currents, upwelling, and mixing—and biogeochemical behaviors, including air–sea CO_2 exchange and biological activity. Moreover, since many observational datasets and ocean carbon products align with regional scales, basin-based flux estimation ensures greater consistency. We examined the seasonal variability and mean state of global CO_2 fluxes, excluding regions where flux sign reverses across seasons—an effect that may introduce substantial uncertainty in model–data comparisons—with particular emphasis on areas exhibiting the strongest oceanic CO_2 flux signals. Some uncertainties in the assimilation dataset arise from factors such as anthropogenic influences and ice melt; therefore, following Fay et al. (2024), this study excludes the coastal ocean and high-latitude sea regions from the model comparison.

Figure 2c highlights the positive and negative CO_2 flux in the Pacific using red dashed lines, while black dashed lines denote other significant regions. Based on these highlighted areas, Fig. 2d highlights 12 key regions of high air–sea CO_2 flux variability identified by NOAA CT2022. These are selected from the 30 ocean basins defined in the CT2022 model documentation (Jacobson et al., 2023) for optimizing flux inversions. These regions include: (1) Pacific Ocean – Northwestern Pacific (NWP), Eastern Equatorial Pacific (EEP), Northeastern Pacific (NEP), South Pacific Ocean 1 (SPO1), and South Pacific Ocean 2 (SPO2); (2) Indian Ocean – North Indian Ocean (NIO), South Indian Ocean 1 (SIO1), and South Indian Ocean 2 (SIO2); and (3) Atlantic Ocean – North Atlantic Ocean 1 (NAO1), North Atlantic Ocean 2 (NAO2), Equatorial Atlantic Ocean (EAO), and South Atlantic Ocean (SAO).

3. Results

3.1 The climatological mean and seasonal variations of air–sea CO_2 flux

We use the traditional air–sea CO_2 flux bulk formula (Eq. 1) in CESM1.2.2 while also incorporating the effects of waves and bubble-mediated processes with $K_{w,660}$, which is parameterized based on u_*, SST, and H_s (Eq. 3). Figure 2a–c compares the climatological mean ocean CO_2 flux (mol m^{-2} yr^{-1}; shaded) and the monthly standard deviation (SD; contours) among B–CTL, POP2–waves, and NOAA CT2022. Overall, the spatial distribution of the model-simulated CO_2 flux is broadly consistent with that of CT2022, with most differences less than 0.5 (mol m^{-2} yr^{-1}) shown in white (Fig. 2e–f), although some discrepancies persist. The primary positive and negative air–sea CO_2 flux patterns in the Pacific simulated by the POP2–waves experiment more closely resemble those in NOAA CT2022 than those in B–CTL, although the POP2–waves experiment exhibits a larger monthly SD than B–CTL over both the Pacific and Indian Oceans.

For the analysis of our results, this study categorized the 12 regions into two groups: those demonstrating close agreement with NOAA CT2022 (9 regions) and those exhibiting significant discrepancies (3 regions). Figure 3 presents a close agreement between the model-simulated CO_2 fluxes and the NOAA CT2022 dataset across the NWP, EEP, NEP, SPO1, NIO, SIO1, NAO1, EAO, and SAO. Monthly mean values for B–CTL (black dashed), POP2–waves (red solid), and NOAA CT2022 (blue solid) are plotted with corresponding standard deviations (SD) shown as colored bars. The POP2–waves simulation generally exhibits higher SD than B–CTL, indicating greater seasonal variability. While typically below 3 mol m^{-2} yr^{-1}, the SD peaks during boreal winter, driven by intense negative air–sea CO_2 fluxes in high-latitude Northern Hemisphere regions such as the NWP, NEP, and NAO1. In contrast, the Southern Hemisphere exhibits large monthly SD alongside relatively strong negative air–sea CO_2

flux during the boreal summer in regions such as SPO1, SIO1, and SAO. The monthly SD of NOAA CT2022 exhibits substantial regional variability, with values in the NWP, EEP, and NAO1 regions exceeding those of both the POP2–waves and B–CTL simulations.

Three regions—SPO2, SIO2, and NAO2—exhibit model discrepancies when compared with NOAA CT2022 (Fig. 4), which are not attributable to wave effects or the CO_2 flux bulk formula. In NAO2, both B–CTL and POP2–waves show seasonal variations similar to those in NAO1, with strong negative air–sea CO_2 flux during the boreal winter, whereas NOAA CT2022 displays the opposite seasonal pattern in this region. A similar pattern is observed in SPO2, where the seasonal variations in both B–CTL and POP2–waves resemble those in SPO1 but contrast with the trend shown by NOAA CT2022.

3.2 The relationship between U_{10} and $K_{w,660}$ in two regions with contrasting wind speed regimes

To demonstrate that the sea state–dependent $K_{w,660}$ (Deike and Melville, 2018) provides a more suitable estimate of CO_2 flux than the wind-only $K_{w,660}$ (Wanninkhof, 1992) under high-wind conditions, we selected two regions with contrasting wind regimes: (a) the WP denotes the Western Pacific region (160–180°E, 35–40°N), where more than 30% of U_{10} exceeds 10 m s^{-1}, and (b) the EP denotes the Equatorial Pacific region (230–250°E, 0–5°S), where all U_{10} values are below 10 m s^{-1}. These regions also exhibit stable and significantly positive or negative oceanic CO_2 fluxes, enabling a comparison of the correlation between $K_{w,660}$ and U_{10}, as shown in Fig. 5a and 5b. Gray open circles represent $K_{w,660}$ calculated using the Wanninkhof (1992) 10-m wind speed equation (B–CTL) with their simple linear regression (SLR) and squared correlation coefficient (R^2) shown in black line and text. Green open squares represent

POP2–waves data for H_s < 1.5m (normal conditions) with the orange solid line and text indicating its SLR and R^2, while blue dots denote cases where H_s > 1.5 m (enhanced conditions) with the red solid line and text depicting their SLR and R^2.

Generally, the B–CTL data shows higher R^2 but lower $K_{w,660}$ values compared to POP2–waves $K_{w,660}$ across all WP and EP. POP2–waves exhibits a slightly lower R^2 than B–CTL due to greater deviations between $K_{w,660}$ and U_{10}, particularly at higher surface wind speeds, consistent with the findings of Gutiérrez-Loza et al. (2022) under conditions where H_s > 1.5 m. While the relationship between $K_{w,660}$ and U_{10}—when based on monthly normal conditions means (H_s < 1.5m) and daily data filtered for Hs>1.5m (enhanced conditions) and then aggregated into 30-year monthly averages—substantially diminishes differences in $K_{w,660}$ at the same U_{10}. However, short-term (30-min) observations indicate that $K_{w,660}$ can be up to twice as high under similar wind speeds (Gutiérrez-Loza et al., 2022, Fig. 7). Zhou et al. (2023) indicated that the wind-only formula for gas transfer velocity tends to underestimate values when U_{10} exceeds 10 m s^{-1}, and that enhanced gas transfer velocity frequently occurs under conditions of strong wave breaking and high significant wave height. Divergence between the models becomes significant when U_{10} exceed 12 m s^{-1} over the WP (Fig. 5a); whereas over the EP, the convergence of $K_{w,660}$ estimates is most notable around U_{10} = 9 m s^{-1} (Fig. 5b), suggesting that mid-range wind speeds dominate the EP flux signal.

Figs. 5c and 5d display the monthly mean values of $K_{w,660}$ for WP and EP, respectively. Red, orange solid, and black dotted lines/texts indicate POP2–waves (H_s > 1.5 m), average of all POP2–waves data, and B–CTL, respectively. The bar graph illustrates the monthly SD values. Figure 5c shows that WP cases with H_s > 1.5 m have monthly data available except in August and October, and their $K_{w,660}$ values are higher than those the averaged values from POP2–waves and B–CTL. In contrast, EP shows H_s > 1.5 m data only during the summer months (July to October), and the

corresponding $K_{w,660}$ values are also higher than those from POP2–waves and B–CTL. The percentage of monthly SD in the bar graph indicates no significant differences between H_s > 1.5 m data and POP2–waves experiments in the WP, while the $K_{w,660}$ difference between the two datasets from January to May remains small because the average H_s during this period exceeds 1.5 m. However, in EP, a significant difference is observed between the H_s > 1.5 m condition and the average in POP2–waves from July to September.

3.3 Regression of CO_2 flux against U_{10} under high-wind conditions

The wind-only parameterization of gas transfer velocity tends to underestimate values when U_{10} > 10 m s^{-1} or H_s > 1.5 m (e.g., Gutiérrez-Loza et al., 2022; Zhou et al., 2023). Accordingly, Fig. 5 presents scatter plots of CO_2 flux from B–CTL and POP2–waves experiment against U_{10} (for U_{10} > 10 m s^{-1}) over the WP region (160–180°E, 35–40°N) to compare fluxes estimated with wind-only $K_{w,660}$ and wave-modified $K_{w,660}$. High-wind conditions over the WP occur primarily in winter (42% valid data), and the associated low ocean surface temperatures further enhance CO_2 solubility. The slopes of the regression equations (–0.77 in B–CTL and –1.40 in POP2–waves) and the mean CO_2 fluxes (Y_{avg}: –6.35 in B–CTL and –6.97 in POP2–waves) both indicate that POP2–waves simulates stronger negative air–sea CO_2 fluxes in the WP region under higher wind speeds. The correlation coefficient (R) of POP2–waves is higher than that of B–CTL, indicating that the sea state–dependent $K_{w,660}$ provides a more suitable estimate of CO_2 flux than the wind-only $K_{w,660}$ under high-wind conditions, consistent with the findings of Gutiérrez-Loza et al. (2022) and Zhou et al. (2023). The average air–sea CO_2 flux in B–CTL over the WP during DJF and JJA is −0.021 and −0.004 (mol m^{-2} yr^{-1}), respectively. Meanwhile, POP2–waves shows only slight changes of −0.001 and +0.002 (mol m^{-2} yr^{-1}) than B–CTL

during DJF and JJA, respectively (not show). This indicates that when U_{10} > 10 m s^{-1}, the air–sea CO_2 flux is significantly greater than the average value.

3.4 Analysis of surface fields and $K_{w,660}$ component in POP2–waves and B–CTL

Figures 7a presents the near-surface fields along with sea level pressure (PSL), U_{10}, and H_s, all of which are factors influencing $K_{w,660}$ in the model. The region with H_s > 1.5 m is generally situated where U_{10} > 8 m s^{-1} and lies south of the high PSL region. Johansson et al. (2022) reported that H_s generally increases with wind speed, but the relationship is strongly modulated by wind direction and regional conditions, leading to spatially variable and nonlinear wind–wave coupling. The climatological U_{10} is shown as shaded colors in Fig. 7a using a high-contrast color bar, with spatial patterns similar to Reichl and Deike (2020), while the H_s contours in Fig. 7b are also consistent with those presented in Reichl and Deike (2020). Similarly, the ratio of $K_{wB,660}/K_{w,660}$ in POP2–waves greater than 0.5 (yellow shaded areas in Fig. 7b) mostly occurs in regions where H_s > 1.5 m. However, high H_s does not always correspond to a higher $K_{wB,660}/K_{w,660}$ in POP2–waves, for example, in the North Pacific. Deike and Melville (2018) demonstrated that the bubble contribution to CO_2 transfer exceeds 40% when the U_{10} is ≥ 10 m s^{-1}. The bubble contribution to the total gas transfer velocity ($K_{wB,660}/K_{w,660}$) in POP2–waves is approximately 38%, which is slightly higher than ~30% reported by Reichl and Deike (2020). This discrepancy may be attributed to differences in the A_B coefficients used in this study compared to previous work. The coefficient in the sea-state formulation (A_B in Eq. (3)) is derived from field data, where gas transfer velocity is estimated from flux measurements using eddy covariance methods (Reichl and Deike, 2020; Brumer et al., 2017).

The contours in Fig. 7c shows that the larger differences in $K_{w,660}$ (POP2–waves − B–CTL) are mainly distributed in regions with higher H_s, particularly within 30°N–

30°S. Although U_{10} in the Indian Ocean and tropical Pacific are relatively low (< 5 m s^{-1}; Fig. 7a), the $K_{w,660}$ values in POP2–waves are still about 9 cm hr^{-1} higher than those in B–CTL. In these regions, the POP2-waves enhanced $K_{w,660}$ is primarily dominated by the non-bubble-mediated component ($K_{wNB,660}$), as shown in Fig. 7d. Although H_s is also large in the Southern Ocean (Fig. 7b), it does not contribute substantially to the $K_{w,660}$ difference between POP2–waves and B–CTL because the high U_{10} in this region (Fig. 7a) already produces large $K_{w,660}$ values through the empirical formulation of Wanninkhof (1992). The spatial distribution of B–CTL $K_{w,660}$ (shaded) and the contours difference $K_{w,660}$ (POP2–waves − B–CTL) shown in Fig. 7c is also similar to Reichl and Deike (2020). B–CTL $K_{w,660}$ and POP2–waves $K_{w,660}$ exhibit similar spatial distributions, with 30-year mean values of 17.0 cm hr^{-1} and 22.7 cm hr^{-1}, respectively, despite using different input parameters (U_{10} vs. $u*$ and H_s). Aside from the polar regions, $K_{w,660}$ in the POP2–waves coupled model is greater than that in B–CTL with the largest differences occurring in the tropics (Fig. 7c). It is interesting to examine whether the non-bubble ($K_{wNB,660}$) or bubble ($K_{wB,660}$) component dominates the POP2–waves $K_{w,660}$ across the global ocean. Figure 7d shows $K_{wNB,660}$ as shaded colors and the difference between $K_{wNB,660}$ and $K_{wB,660}$ as contours. The differences indicate that $K_{wB,660} > K_{wNB,660}$ in regions with high H_s (Fig. 7b contours), whereas $K_{wB,660} < K_{wNB,660}$ in regions where U_{10} is below 7 m s^{-1} (Fig. 7a shaded).

4. Discussion

4.1 Mean State and model differences in pCO_2^w and surface pH

Several recent studies have estimated the air–sea CO_2 flux using Eq. (1), although current $K_{w,660}$ parameterizations in global models (Table 1) still rely exclusively on the neutral U_{10} (e.g., Chikamoto and DiNezio, 2021; Danabasoglu et al., 2020; Seland et

al., 2020; Mauritsen et al., 2019; Ziehn et al., 2020; Lovato et al., 2022; Sigmond et al., 2023). A few recent studies have quantified wave effects on air–sea CO_2 flux and ocean carbon storage using wind–wave–bubble gas transfer formulations in OGCMs (Table 1) such as MOM6–COBALTv2 (Rustogi et al., 2025) and NEMO–PISCES (Wu et al., 2025). Wu et al. (2025) further emphasize the need to include wave-related processes in Earth System Models to better represent the carbon cycle.

Some studies incorporate wave effects following Deike and Melville (2018), using the Surface Ocean CO_2 Atlas (SOCAT) database (Bakker et al., 2016) to estimate air–sea CO_2 fluxes. In these approaches, air–sea CO_2 flux is treated independently of pCO_2^w values and ocean pH, with no feedback between them.

Figure 8 illustrates the means and differences in the spatial distribution of pCO_2^w and pH in the B–CTL and alongside the respective differences between the POP2–waves and B–CTL experiments. In B–CTL, high pCO_2^w is concentrated in the equatorial eastern Pacific (EEP), contributing to a larger oceanic CO_2 source (Fig. 2a). In contrast, low pCO_2^w is found in the high-latitude regions of the Pacific and Atlantic (e.g., NWP, NEP, NAO1, and NAO2), resulting in strong negative air–sea CO_2 fluxes (Fig. 2a). The standard deviation of pCO_2^w in the B–CTL simulation, indicated by the contours in Fig. 8a, fluctuates between 10 and 30 ppm over the study period.

In the CESM1 framework of the B_2000_CAM5 compsets, atmospheric pCO_2^a is held constant (367 ppm). The pCO_2^w in the EP exceeds 440 ppm, indicating an air–sea $dpCO_2$ greater than 73 ppm in B–CTL (109.8 and 92.7 ppm during DJF and JJA, respectively), whereas the pCO_2^w in the WP is below 320 ppm, indicating an air–sea $dpCO_2$ lower than −47 ppm (−53.4 and −31.4 ppm during DJF and JJA, respectively). Notably, POP2–waves reduces the high pCO_2^w by more than 10 ppm over the EEP and increases the low pCO_2^w in other regions (Fig. 8b). Consequently, in positive (negative) air–sea CO_2 flux regions, the POP2-waves coupled model decreases (increases) pCO_2^w,

thereby reducing the magnitude of the air–sea dpCO_2. The SD of the pCO_2^w difference between POP2–waves and B–CTL varies significantly in EEP, while SD changes in other regions are less pronounced.

The marine carbonic acid system is a nonlinear, coupled system governed by CO_2 dissolution equilibrium, $(CO_{2(aq)} + H_2O \overset{K_H}{\leftrightarrow} H_2CO_{3(aq)})$, where the Henry's constant (K_H) for CO_2 in water at 25°C is approximately 3.4 x 10^{-2} (m/atm), two-step dissociation reactions, and the conservation of the total dissolved inorganic carbon (DIC) and total alkalinity (TA), ultimately determining pH and the distribution of carbonate species. The H_2CO_3 has two hydrogen ions and dissociates in two steps:

$$H_2CO_3 \overset{K_{a1}}{\longleftrightarrow} H^+ + HCO_3^- \qquad K_{a1} = 4.4\times10^{-7} \tag{4}$$

$$HCO_3^- \overset{K_{a2}}{\longleftrightarrow} H^+ + CO_3^{2-} \qquad K_{a2} = 4.7\times10^{-11} \tag{5}$$

The DIC can be expressed as

$$\begin{aligned} DIC &= [H_2CO_3] + [HCO_3^-] + [CO_3^{2-}] \\ &= K_H pCO_2^w + \frac{K_{a1} K_H pCO_2^w}{[H^+]} + \frac{K_{a1} K_{a2} K_H pCO_2^w}{[H^+]^2} \\ &= K_H pCO_2^w \left(1 + \frac{K_{a1}}{[H^+]} + \frac{K_{a1} K_{a2}}{[H^+]^2}\right) \\ &= K_H pCO_2^w ([H^+]^2 + K_{a1}[H^+] + K_{a1} K_{a2})/[H^+]^2 \end{aligned} \tag{6}$$

The marine carbonate system describes the distribution of DIC among its chemical species in seawater and is jointly governed by TA and pH. From Eq. (6), if the oceanic pCO_2^w and pH are known, the DIC can be determined, conversely, pCO_2^w can be inferred from DIC. TA is defined as the sum of the proton-neutralizing capacities of all weak acid anions in seawater (Dickson, 1981) and can be expressed as:

$TA=[HCO_3^-]+2[CO_3^{2-}]+[B(OH)_4^-]+[OH^-]+[HPO_4^{2-}]+2[PO_4^{3-}]+[SiO(OH)_3]+[NH_3]+[HS^-]-[H^+]-[H_3PO_4]$. In the POP2-waves framework, TA, pH and biogeochemistry are also used to calculate pCO_2^w.

When TA increases, the seawater becomes more alkaline, leading to an increase in CO_3^{2-} concentration and enhanced buffering of hydrogen ions. As a result, the $[H^+]$ decreases, causing pH to rise and increasing the ocean's capacity to absorb CO_2. Conversely, when TA decreases, the buffering capacity weakens, $[H^+]$ increases, pH decreases, and the ocean becomes more acidic with a reduced ability to uptake CO_2.

The biogeochemical module of POP2 (MARBL) updates TA in each grid cell by solving a coupled transport–reaction equation (Long et al., 2021). The average pH of the ocean is currently around 8.1 in negative air–sea CO_2 flux regions (e.g., WP) and 8.0 in positive air–sea CO_2 flux regions (e.g., EP, Fig. 8c), reflecting slightly alkaline conditions. Within the DIC system, bicarbonate ions (HCO_3^-) are the dominant species because the prevailing pH lies between pK_{a1} and pK_{a2}. However, continued uptake of atmospheric CO_2 drives a decline in pH, a process termed ocean acidification. Our study highlights that wave-induced $K_{w,660}$ significantly influences the marine CO_2 system, altering alkalinity, pH, and carbonate speciation. These chemical changes, in turn, provide a feedback mechanism that modulates the overall dynamics of the air–sea CO_2 flux. In other words, perturbations in $K_{w,660}$ influence both $dpCO_2$ and air–sea CO_2 flux in the Earth System Model. This POP2–waves coupled behavior differs from traditional approaches that treat wave-induced $K_{w,660}$ and $dpCO_2$ as independent variables when estimating air–sea CO_2 flux (e.g., Reichl and Deike, 2020).

Ocean pH and pCO_2^w are strongly negatively correlated (Macovei et al. 2021), with low pH values observed in the equatorial eastern Pacific (Fig. 8c), resulting from high pCO_2^w concentrations in that region (Fig. 8a). Slightly higher pH values are observed in regions with lower pCO_2^w, such as the NWP, NEP, NAO1, and NAO2. Rustogi et al. (2025) indicate that faster equilibration of oceanic pCO_2 in the wind–wave–bubble simulation, driven by enhanced gas exchange, reduces the air–sea $dpCO_2$. This pCO_2 feedback is strongest in the extratropics, where it suppresses CO_2 uptake.

Our POP2–waves experiment shows a similar response, with increasing pCO_2 (Fig. 8b) and hydrogen ion concentration, accompanied by decreasing pH (Fig. 8d) in the extratropics. Accounting for wave effects results in simulated pH differences of approximately + (-) 0.01 in positive (negative) air–sea CO_2 flux regions (Fig. 8d). This suggests that including this mechanism mitigates acidification in the equatorial Pacific but enhances ocean acidification in the NWP, NEP, NAO1, and NAO2 regions (Fig. 8d). Rustogi et al. (2025) also showed that the effects of ΔK_w (between wave-induced and based on U_{10}) and $\Delta dpCO_2$ partially offset each other, although the ΔK_w effect is generally 20%–30% stronger than the counteracting $\Delta dpCO_2$ effect, explaining the modest increase in both positive and negative air–sea CO_2 fluxes in the wave effect simulation.

4.2 Impact of air–sea $dpCO_2$, $K_{w,660}$, SST, and pH on air–sea CO_2 flux

To determine which factor is directly associated with air–sea CO_2 flux, Fig. 9 presents the linear regression coefficients (LRC) between air–sea CO_2 flux and various normalized variables: air–sea $dpCO_2$ (Fig. 9a), $K_{w,660}$ (Fig. 9b), SST (Fig. 9c), and pH (Fig. 9d). To confirm the statistical significance of the variables, we first conducted a t-test (at the 95% confidence level). Subsequently, we standardized both the air–sea CO_2 flux and the relevant variables into anomalies with a mean of 0 and a standard deviation of 1, thereby removing the influence of differing units and enabling comparison on a common scale. This allows the LRC to range between −1 and +1. Here, we do not delve into the complex chemical and biochemical mechanisms in carbonate species; although, the influence of carbonate species composition, including TA, and dissolved inorganic carbon (DIC), on pCO_2^w is greater than that of solubility changes driven by sea surface salinity and SST (Koseki et al., 2023).

Among these factors, air–sea $dpCO_2$ and air–sea CO_2 flux exhibit the strongest positive LRC (0.6–0.8) across the global ocean, with the ocean acting as a source or sink of CO_2 depending on whether the air–sea $dpCO_2$ is positive or negative. Additionally, wave effects increase the LRC by approximately 0.1 to 0.2, particularly in strong positive or negative air–sea CO_2 flux regions. There is a clear positive (negative) LRC between $K_{w,660}$ and air–sea CO_2 flux in positive (negative) air–sea CO_2 flux regions. Furthermore, wave effects reduce the absolute LRC between $K_{w,660}$ and air–sea CO_2 flux in both positive and negative air–sea CO_2 flux regions (Fig. 9b), indicating that wave-influenced CO_2 flux is less correlated with $K_{w,660}$ and more closely linked to air–sea $dpCO_2$, after considering interactions between modeled air–sea CO_2 flux and the ocean carbonate-pH system.

In contrast to the former, there is a clear positive (negative) LRC between SST and CO_2 flux in negative (positive) air–sea CO_2 flux regions (Fig. 9c). $K_{w,660}$ and SST are negatively correlated, reflecting the latitudinal gradient where colder, high-latitude waters are associated with more intense sea states and higher $K_{w,660}$. This pattern occurs because lower temperatures in high-latitude regions increase CO_2 solubility, thereby enhancing oceanic uptake. Conversely, higher SST in tropical regions reduce solubility, promoting CO_2 outgassing. As SST increases, CO_2 molecules become more mobile in seawater, enhancing diffusion and reducing the Schmidt number ($Sc=\nu/D$, the ratio of kinematic viscosity to the diffusion coefficient). Because $K_{w,660}$ is parameterized as $Sc^{-0.5}$, a decrease in Sc leads to an increase in $K_{w,660}$ and air–sea CO_2 flux. Fay et al. (2024) attributed the variations in air–sea CO_2 fluxes to a combination of factors, including fluctuations in SST, biological uptake of CO_2, and variations in mixing and wind speeds. Wave effects only slightly reduce the LRC between SST and CO_2 flux—by approximately 0.1—in the tropics, with negligible differences observed in other regions. The strong negative correlation between ocean pH and pCO_2^w is attributed to

the acid dissociation constants of H_2CO_3 (Fig. 8a and 8c), which govern the relationship between dissolved CO_2 and hydrogen ion concentration (Williams et al., 2017). When seawater pH decreases, the concentration of H^+ increases. Carbonate ions (CO_3^{2-}) react with these excess H^+, reducing the ocean's buffering capacity for CO_2 uptake. As a result, pCO_2^w increases and $dpCO_2$ decreases, leading to a reduction in the air–sea CO_2 flux into the ocean. pH and CO_2 flux exhibit strong negative LRC (< –0.9) across the global ocean, with only a few exceptions in the EEP and along the Arctic margins (Fig. 9d). Wave effects again only slightly reduce the LRC between pH and CO_2 flux in the EEP—by approximately 0.1.

4.3 Uncertainty arising from the absence of interactions between air–sea CO_2 flux and the ocean carbonate–pH system

Rustogi et al. (2025) indicate that as pCO_2^w responds to changes in DIC and alkalinity, the air–sea $dpCO_2$ is partially reduced. This induces a negative feedback loop, whereby enhanced CO_2 uptake (or outgassing) is damped by chemical re-equilibration within the marine carbonate system, consistent with the findings of this study. To assess the uncertainty in CO_2 flux resulting from the absence of interactions between air–sea CO_2 flux and the ocean carbonate–pH system (i.e., the lack of $dpCO_2$-driven negative feedback), Fig. 10a presents the air–sea CO_2 flux calculated using air–sea $dpCO_2$ values (from B–CTL) and $K_{w,660}$ incorporating wave effects (from POP2–waves), with shading representing the mean (labeled as "no $dpCO_2$ feedback") and contours indicating their SD. Only data significant at a 95% confidence level of air–sea CO_2 flux difference between "no $dpCO_2$ feedback" and POP2–waves are shown in Fig. 10b. Compared to Fig. 2b, the CO_2 flux in the "no $dpCO_2$ feedback" case is stronger than that in the POP2–waves simulation across both positive and negative air–sea CO_2 flux regions, and is accompanied by a larger SD. The most pronounced differences occur in Pacific regions

546 with both positive and negative air–sea CO_2 fluxes; however, some areas (e.g., NEP,
547 SIO2, and SPO2) do not reach the 95% confidence threshold.

548 Rustogi et al. (2025) demonstrate that while wave-enhanced $K_{w,660}$ accelerates
549 local air–sea CO_2 exchange, it simultaneously reduces the air–sea $dpCO_2$. In this study,
550 we refer to this process as the ocean's buffering capacity which includes the interactions
551 between CO_2 flux (estimated from $K_{w,660}$ and the ocean carbonate–pH system.
552 Incorporating wave effects mitigates pH acidification and reduces air–sea $dpCO_2$ over
553 positive air–sea CO_2 flux regions, while relatively higher pH levels enhance the ocean's
554 capacity to absorb additional atmospheric CO_2 in regions characterized by negative air–
555 sea CO_2 flux region in the coupled POP2–waves model. (Fig. 8b and 8d). In contrast,
556 the "lack of $dpCO_2$-driven negative feedback" case, which does not include real ocean
557 buffering effects, allows positive air–sea CO_2 flux regions to release excess CO_2 into
558 the atmosphere (> 0.4 mol m^{-2} yr^{-1}) while simultaneously enhancing excess CO_2 uptake
559 (< -0.4 mol m^{-2} yr^{-1}) in negative air–sea CO_2 flux regions (Fig. 10b) compared to the
560 coupled POP2–waves model.

561

562 **5 Conclusions**

563 The primary contribution of this study lies in its online coupling framework in
564 Earth System Model, which explicitly incorporates wave effects into air–sea CO_2 flux
565 simulations, thereby capturing the ocean's buffering capacity with $dpCO_2$-driven
566 negative feedback in the ocean carbonate-pH system. In contrast, treating $dpCO_2$ and
567 wave-induced $K_{w,660}$ independently leads to a substantial overestimation of air–sea CO_2
568 fluxes when compared to online coupling POP2-waves simulations (Fig. 10).

569 Coupling a wave model into an ocean circulation model to simulate air–sea CO_2
570 flux presents substantial challenges arising from multi-scale physical processes, cross-

component coupling, and nonlinear carbon cycle feedbacks. The integration of wave effects into ocean biogeochemical models involves three core challenges:

1. Technical implementation: Overcoming coordinate interpolation issues, boundary discontinuities in wave energy, and MPI parallelization (Fig. 1).
2. Interdisciplinary analysis: Blending kinematic, thermodynamic, and biogeochemical frameworks.
3. Validation constraints: Navigating sparse and inconsistent observational data, where air–sea CO_2 fluxes must be indirectly inferred from atmospheric inversions (e.g., NOAA CT2022), ships, and buoys.

Within the POP2–waves coupled model, $K_{w,660}$ is determined using the parameterization of Deike and Melville (2018), which attributes bubble-mediated transfer to the combined effects of friction velocity and significant wave height. Furthermore, Wu et al. (2025) also investigated the influence of these mechanisms within a global ocean coupled model, aiming to better capture the indirect effects of changes in surface DIC—driven by air–sea CO_2 flux—on the flux itself. In the 12 key regions exhibiting significant air–sea CO_2 flux variability identified by NOAA CT2022, the POP2–waves experiment simulates patterns that more closely resemble NOAA CT2022 than B–CTL simulation (Figs. 2 and 3), although notable discrepancies persist in three regions: SPO2, SIO2, and NAO2 (Fig. 4).

Significant deviations between POP2–waves and B–CTL emerge in $K_{w,660}$–U_{10} scatter plots specifically when H_s exceeds 1.5 m (Fig. 5a–b), consistent with Gutiérrez-Loza et al. (2022), indicating that POP2–waves coupled model exhibits a stronger CO_2 flux than B–CTL under high U_{10} and H_s (Fig. 6). In addition, the bubble contribution to the total gas transfer velocity ($K_{wB,660}/K_{w,660}$) in POP2–waves averages approximately 38% across the entire space–time domain (Fig. 7b), slightly exceeding the ~30% reported by Reichl and Deike (2020). These high $K_{wB,660}/K_{w,660}$ regions align with areas

of elevated H_s and U_{10}. Furthermore, our results indicate that bubbles account for up to 41.3% of the total air–sea CO_2 flux, which is consistent with the ~40% contribution reported by both Zhou et al. (2023) and Reichl and Deike (2020).

POP2–waves reduces high pCO_2^w over the positive air–sea CO_2 flux regions and increases low pCO_2^w elsewhere (Fig. 8b), resulting in pH shifts of roughly ± 0.01 that align with regional air–sea CO_2 signs (Fig. 8d). On a global scale, air–sea $dpCO_2$ (pH) displays the strongest positive (negative) regression coefficients with the flux (Figs. 9a, d). Additionally, $K_{w,660}$ scales positively with the absolute air–sea CO_2 flux, whereas SST demonstrates an inverse relationship to $K_{w,660}$ sensitivity (Figs. 9b, c).

POP2–waves show increases of 11.8%, 41.6%, and 1.8% in the air–sea negative CO_2 flux regions, positive CO_2 flux regions, and the global ocean carbon sink, respectively, compared to B–CTL. Consequently, although wave-induced enhancements in $K_{w,660}$ increase instantaneous air–sea CO_2 flux, the coupled carbonate–pH system limits the net long-term impact through this pCO_2-driven feedback (Rustogi et al., 2025). This explains why local increases in CO_2 flux do not translate proportionally into global mean changes in the ocean carbon sink.

Finally, the effects of the $K_{w,660}$ bulk formula (Wanninkhof et al., 1992) and wave dynamics (Deike and Melville, 2018) on air–sea CO_2 flux (arrows), surface pH (tube colors indicator), and air–sea $dpCO_2$ (circle markers) in the strongest negative air–sea CO_2 flux (WP) and positive air–sea CO_2 flux (EP) regions during the DJF and JJA seasons are schematically summarized in Fig. 11. B–CTL is illustrated in gray with black text, while differences between POP2–waves and B–CTL are highlighted in red. Each panel features the air–sea interface, with ocean color shading representing relative SST levels across seasons, and the SST value displayed in the lower-left corner of each panel. The B–CTL model captures a pronounced seasonal contrast in WP air–sea CO_2 fluxes, with strong uptake in DJF that is heavily suppressed in JJA by SST-driven

reductions in solubility. As illustrated by the seasonal changes in air–sea $dpCO_2$ (Figs. 11a and 11c), a negative feedback loop in the POP2–waves model acts to modulate the overall air–sea CO_2 flux. In contrast, the EP region exhibits lower pH than the WP and acts as a strong CO_2 source in both DJF and JJA (Fig. 11b and 11d), with no obvious seasonal variation (consistent with Fay et al., 2024).

Code and data availability. The model code of POP2–waves coupled model is available at https://doi.org/10.5281/zenodo.15795234 (Lan, 2025). Input data of POP2–waves using the climatological Hadley Centre Sea Ice and Sea Surface Temperature dataset, including 30-year numerical experiments, are available at https://doi.org/10.5281/zenodo.5510795 (Lan et al., 2021). CarbonTracker CT2022 data are provided by the National Oceanic and Atmospheric Administration (NOAA) and available from Global Monitoring Laboratory https://gml.noaa.gov/aftp/products/carbontracker/co2/CT2022/ (Jacobson et al., 2023).

Author contributions. YYL is the sole developer of the POP2–waves coupled model and writes the majority part of the paper. HHH provides computational support and analysis suggestions. WLL supports reorganization and offers analytical recommendations and SC offers a non-parallel wave module as part of the POM source code.

Competing interests. The authors declare that they have no conflict of interest.

Acknowledgements. Our deepest gratitude goes to the editors and anonymous reviewers for their careful work and thoughtful suggestions that have helped improve this paper substantially. We would like to thank NOAA GML (Boulder, Colorado, USA) for

providing the CarbonTracker CT2022 data from the website at http://carbontracker.noaa.gov (last access: 20 May 2026). We sincerely thank the National Center for Atmospheric Research (NCAR) and their Atmosphere Model Working Group (AMWG) for release CESM1.2.2. We are also grateful to the National Center for High- performance Computing, Taiwan for providing the facilities for the computational procedures for running POP2-waves simulations. Thanks, ChatGPT for correcting the English grammar.

Financial support. This research received funding from the Taiwan National Science and Technology Council under Grants NSTC 112-2111-M-001-008 and MOST 111-2123-M-001-007, as well as support from the Academia Sinica Grand Challenge Program in Taiwan under Grant AS-GCP-112-M03.

Reference

Akhand, A., Chanda, A., Watanabe, K., Das, S., Tokoro, T., Hazra, S., and Kuwae, T.: Reduction in riverine freshwater supply changes inorganic and organic carbon dynamics and air-water CO_2 fluxes in a tropical mangrove dominated estuary, J. Geophys. Res. G: Biogeosciences, 126, e2020JG006144, https://doi.org/10.1029/2020JG006144, 2021.

Andreas, E., Vlahos, P., and Monahan, E.: The potential role of sea spray droplets in facilitating air–sea gas transfer, in: IOP conference series: earth and environmental science, Vol. 35, p. 012003, IOP Publishing, https://doi.org/10.1088/1755-1315/35/1/012003, 2016.

Bakker, D. C. E., Pfeil, B., Landa, C. S., Metzl, N., O'Brien, K. M., Olsen, A., Smith, K., Cosca, C., Harasawa, S., Jones, S. D., Nakaoka, S., Nojiri, Y., Schuster, U., Steinhoff, T., Sweeney, C., Takahashi, T., Tilbrook, B., Wada, C., Wanninkhof, R., Alin, S. R., Balestrini, C. F., Barbero, L., Bates, N. R., Bianchi, A. A., Bonou, F., Boutin, J., Bozec, Y., Burger, E. F., Cai, W.-J., Castle, R. D., Chen, L., Chierici, M., Currie, K., Evans, W., Featherstone, C., Feely, R. A., Fransson, A., Goyet, C., Greenwood, N., Gregor, L., Hankin, S., Hardman-Mountford, N. J., Harlay, J., Hauck, J., Hoppema, M., Humphreys, M. P., Hunt, C. W., Huss, B., Ibánhez, J. S. P., Johannessen, T., Keeling, R., Kitidis, V., Körtzinger, A., Kozyr, A., Krasakopoulou, E., Kuwata, A., Landschützer, P., Lauvset, S. K.,

Lefèvre, N., Lo Monaco, C., Manke, A., Mathis, J. T., Merlivat, L., Millero, F. J., Monteiro, P. M. S., Munro, D. R., Murata, A., Newberger, T., Omar, A. M., Ono, T., Paterson, K., Pearce, D., Pierrot, D., Robbins, L. L., Saito, S., Salisbury, J., Schlitzer, R., Schneider, B., Schweitzer, R., Sieger, R., Skjelvan, I., Sullivan, K. F., Sutherland, S. C., Sutton, A. J., Tadokoro, K., Telszewski, M., Tuma, M., van Heuven, S. M. A. C., Vandemark, D., Ward, B., Watson, A. J., and Xu, S.: A multi-decade record of high-quality fCO_2 data in version 3 of the Surface Ocean CO_2 Atlas (SOCAT), Earth Syst. Sci. Data, 8, 383–413, https://doi.org/10.5194/essd-8-383-2016, 2016.

Bange, H. W., Mongwe, P., Shutler, J. D., Arévalo-Martínez, D. L., Bianchi, D., Lauvset, S. K., Liu, C., Löscher, C. R., Martins, H., Rosentreter, J. A., Schmale, O., Steinhoff, T., Upstill-Goddard, R. C., Wanninkhof, R., Wilson, S. T., and Xie, H.: Advances in understanding of air–sea exchange and cycling of greenhouse gases in the upper ocean, Elem Sci Anth, 12 (1), https://doi.org/10.1525/elementa.2023.00044, 2024.

Behncke, J., Landschützer, P., and Tanhua, T.: A detectable change in the air–sea CO_2 flux estimate from sailboat measurements, Sci. Rep., 14, 3345, https://doi.org/10.1038/s41598-024-53159-0, 2024.

Bell, T. G., Landwehr, S., Miller, S. D., de Bruyn, W. J., Callaghan, A. H., Scanlon, B., Ward, B., Yang, M., and Saltzman, E. S.: Estimation of bubble-mediated air–sea gas exchange from concurrent DMS and CO_2 transfer velocities at intermediate–high wind speeds, Atmos. Chem. Phys., 17, 9019–9033, https://doi.org/10.5194/acp-17-9019-2017, 2017.

Blomquist, B. W,, Brumer, S. E., Fairall, C. W., Huebert, B. J., Zappa, C. J., Brooks, I. M., Yang, M., Bariteau, L., Prytherch, J., Hare, J. E., Czerski, H., Matei, A., and Pascal, R. W.: Wind speed and sea state dependencies of air–sea gas transfer: Results from the High Wind speed Gas exchange Study (HiWinGS), J. Geophys. Res.-Ocean., 122, 8034–8062, https://doi.org/10.1002/2017JC013181, 2017.

Blumberg, A. F., and Mellor, G. L.: A Description of a Three-Dimensional Coastal Ocean Circulation Model, Costal and Estuarine Science, vol. 4, American Geophysical Union, https://doi.org/10.1029/CO004p0001, 1987.

Boucher, O., Servonnat, J., Albright, A. L., Aumont, O., Balkanski, Y., Bastrikov, V., Bekki, S., Bonnet, R., Bony, S., Bopp, L., Braconnot, P., Brockmann, P., Cadule, P., Caubel, A., Cheruy, F., Codron, F., Cozic, A., Cugnet, D., D'Andrea, F., Davini, P., de Lavergne, C., Denvil, S., Deshayes, J., Devilliers, M., Ducharne, A., Dufresne, J.-L., Dupont, E., Éthé, C., Fairhead, L., Falletti, L., Flavoni, S., Foujols, M.-A., Gardoll, S., Gastineau, G., Ghattas, J., Grandpeix, J.-Y., Guenet, B., Guez, Lionel, E., Guilyardi, E., Guimberteau, M.,

Hauglustaine, D., Hourdin, F., Idelkadi, A., Joussaume, S., Kageyama, M., Khodri, M., Krinner, G., Lebas, N., Levavasseur, G., Lévy, C., Li, L., Lott, F., Lurton, T., Luyssaert, S., Madec, G., Madeleine, J.-B., Maignan, F., Marchand, M., Marti, O., Mellul, L., Meurdesoif, Y., Mignot, J., Musat, I., Ottlé, C., Peylin, P., Planton, Y., Polcher, J., Rio, C., Rochetin, N., Rousset, C., Sepulchre, P., Sima, A., Swingedouw, D., Thiéblemont, R., Traore, A. K., Vancoppenolle, M., Vial, J., Vialard, J., Viovy, N., and Vuichard, N.: Presentation and Evaluation of the IPSL-CM6A-LR Climate Model, J. Adv. Model. Earth Sy., 12, e2019MS002010, https://doi.org/10.1029/2019MS002010, 2020.

Brumer, S. E., Zappa, C. J., Blomquist, B. W., Fairall, C. W., Cifuentes-Lorenzen, A., Edson, J. B., Brooks, I. M., and Huebert, B. J.: Wave-related Reynolds number parameterizations of CO_2 and DMS transfer velocities, Geophys. Res. Lett., 44, 9865–9875, https://doi.org/10.1002/2017GL074979, 2017.

Chikamoto, M. O., and DiNezio, P.: Multi-century changes in the ocean carbon cycle controlled by the tropical oceans and the Southern Ocean, Global Biogeochem. Cy., 35, e2021GB007090, https://doi.org/10.1029/2021GB007090, 2021.

Chikamoto, M. O., DiNezio, P., and Lovenduski, N.: Long-term slowdown of ocean carbon uptake by alkalinity dynamics, Geophys. Res. Lett., 50, e2022GL101954, https://doi.org/10.1029/2022GL101954, 2023.

Coggins, A., Watson, A. J., Schuster, U., Mackay, N., King, B., McDonagh, E., and Poulton, A. J.: Surface ocean carbon budget in the 2017 South Georgia diatom bloom: Observations and validation of profiling biogeochemical argo floats, Deep-Sea Res. II: Top. Stud. Oceanogr., 209, 105275. https://doi.org/10.1016/j.dsr2.2023.105275, 2023.

Couldrey, M. P., Oliver, K. I. C., Yool, A., Halloran, P. R., and Achterberg, E. P.: On which timescales do gastransfer velocities control NorthAtlantic CO_2 flux variability?, Global Biogeochem. Cy., 30,787–802, https://doi.org/10.1002/2015GB005267, 2016.

Czerski, H., Brooks, I. M., Gunn, S., Pascal, R., Matei, A., and Blomquist, B.: Ocean bubbles under high wind conditions – Part 2: Bubble size distributions and implications for models of bubble dynamics, Ocean Sci., 18, 587–608, https://doi.org/10.5194/os-18-587-2022, 2022.

Danabasoglu, G., Lamarque, J.-F., Bacmeister, J., Bailey, D. A., DuVivier, A. K., Edwards, J., Emmons, L. K., Fasullo, J., Garcia, R., Gettelman, A., Hannay, C., Holland, M. M., Large, W. G., Lauritzen, P. H., Lawrence, D. M., Lenaerts, J. T. M., Lindsay, K., Lipscomb, W. H., Mills, M. J., Neale, R., Oleson, K. W., Otto-Bliesner, B., Phillips, A. S., Sacks, W., Tilmes, S., van Kampenhout,

776 L., Vertenstein, M., Bertini, A., Dennis, J., Deser, C., Fischer, C.,
777 Fox-Kemper, B., Kay, J. E., Kinnison, D., Kushner, P. J., Larson,
778 V. E., Long, M. C., Mickelson, S., Moore, J. K., Nienhouse, E.,
779 Polvani, L., Rasch, P. J., and Strand, W. G.: The Community Earth
780 System Model Version 2 (CESM2), J. Adv. Model. Earth Sy., 12,
781 e2019MS001916, https://doi.org/10.1029/2019MS001916, 2020.

782 Deike, L., and Melville, W. K.: Gas transfer by breaking waves, Geophys.
783 Res. Lett., 45, 10,482–10,492.
784 https://doi.org/10.1029/2018GL078758, 2018.

785 Deike, L.: Mass transfer at the ocean-atmosphere interface: The role of
786 wave breaking, droplets, and bubbles, Annu. Rev. Fluid Mech, 54,
787 191–224, https://doi.org/10.1146/annurev-fluid-030121-014132,
788 2022.

789 Dickson, A. G.: An exact definition of total alkalinity and a procedure
790 for the estimation of alkalinity and total inorganic carbon from
791 titration data, Deep-Sea Res., 28A (6), 609-623,
792 https://doi.org/10.1016/0198-0149(81)90121-7, 1981.

793 Dong, Y., Yang, M., Bakker, D. C. E., Kitidis, V., and Bell, T. G.:
794 Uncertainties in eddy covariance air–sea CO_2 flux measurements and
795 implications for gas transfer velocity parameterisations, Atmos.
796 Chem. Phys., 21, 8089–8110, https://doi.org/10.5194/acp-21-8089-
797 2021, 2021.

798 Dong, Y., Bakker, D. C. E., Bell, T. G., Huang, B., Landschützer, P.,
799 Liss, P. S., and Yang, M.: Update on the temperature corrections of
800 global air–sea CO_2 flux estimates, Global Biogeochem. Cy., 36,
801 e2022GB007360, https://doi.org/10.1029/2022GB007360, 2022.

802 Edson, J. B., Fairall, C. W., Bariteau, L., Zappa, C. J., Cifuentes-
803 Lorenzen, A., McGillis, W. R., Pezoa, S., Hare, J. E., and Helmig,
804 D.: Direct covariance measurement of CO_2 gas transfer velocity
805 during the 2008 Southern Ocean Gas Exchange Experiment: Wind
806 speed dependency, J. Geophys. Res., 116,
807 https://doi.org/10.1029/2011jc007022, 2011.

808 Fay, A. R., Gregor, L., Landschützer, P., McKinley, G. A., Gruber, N.,
809 Gehlen, M., Iida, Y., Laruelle, G. G., Rödenbeck, C., Roobaert, A.,
810 and Zeng, J.: SeaFlux: harmonization of air–sea CO_2 fluxes from
811 surface pCO_2 data products using a standardized approach, Earth
812 Syst. Sci. Data, 13, 4693–4710, https://doi.org/10.5194/essd-13-
813 4693-2021, 2021.

814 Fay, A. R., Munro, D. R., McKinley, G. A., Pierrot, D., Sutherland, S.
815 C., Sweeney, C., and Wanninkhof, R.: Updated climatological mean
816 ΔfCO_2 and net sea–air CO_2 flux over the global open ocean regions,
817 Earth Syst. Sci. Data, 16, 2123–2139, https://doi.org/10.5194/essd-
818 16-2123-2024, 2024.

819 Friedlingstein, P., Jones, M. W., O'Sullivan, M., Andrew, R. M., Bakker,

D. C. E., Hauck, J., Le Quéré, C., Peters, G. P., Peters, W., Pongratz, J., Sitch, S., Canadell, J. G., Ciais, P., Jackson, R. B., Alin, S. R., Anthoni, P., Bates, N. R., Becker, M., Bellouin, N., Bopp, L., Chau, T. T. T., Chevallier, F., Chini, L. P., Cronin, M., Currie, K. I., Decharme, B., Djeutchouang, L. M., Dou, X., Evans, W., Feely, R. A., Feng, L., Gasser, T., Gilfillan, D., Gkritzalis, T., Grassi, G., Gregor, L., Gruber, N., Gürses, Ö., Harris, I., Houghton, R. A., Hurtt, G. C., Iida, Y., Ilyina, T., Luijkx, I. T., Jain, A., Jones, S. D., Kato, E., Kennedy, D., Klein Goldewijk, K., Knauer, J., Korsbakken, J. I., Körtzinger, A., Landschützer, P., Lauvset, S. K., Lefèvre, N., Lienert, S., Liu, J., Marland, G., McGuire, P. C., Melton, J. R., Munro, D. R., Nabel, J. E. M. S., Nakaoka, S.-I., Niwa, Y., Ono, T., Pierrot, D., Poulter, B., Rehder, G., Resplandy, L., Robertson, E., Rödenbeck, C., Rosan, T. M., Schwinger, J., Schwingshackl, C., Séférian, R., Sutton, A. J., Sweeney, C., Tanhua, T., Tans, P. P., Tian, H., Tilbrook, B., Tubiello, F., van der Werf, G. R., Vuichard, N., Wada, C., Wanninkhof, R., Watson, A. J., Willis, D., Wiltshire, A. J., Yuan, W., Yue, C., Yue, X., Zaehle, S., and Zeng, J.: Global Carbon Budget 2021, Earth Syst. Sci. Data, 14, 1917–2005, https://doi.org/10.5194/essd-14-1917-2022, 2022.

Gray, A. R., Johnson, K. S., Bushinsky, S. M., Riser, S. C., Russell, J. L., Talley, L. D., Wanninkhof, R., Williams, N. L., and Sarmiento, J. L.: Autonomous biogeochemical floats detect significant carbon dioxide outgassing in the high-latitude Southern Ocean, Geophys. Res. Lett., 45(17), 9049–9057, https://doi.org/10.1029/2018GL078013, 2018.

Gutiérrez-Loza, L., Nilsson, E., Wallin, M. B., Sahlée, E., and Rutgersson, A.: On physical mechanisms enhancing air–sea CO_2 exchange, Biogeosciences, 19, 5645–5665, https://doi.org/10.5194/bg-19-5645-2022, 2022.

Hajima, T., Watanabe, M., Yamamoto, A., Tatebe, H., Noguchi, M. A., Abe, M., Ohgaito, R., Ito, A., Yamazaki, D., Okajima, H., Ito, A., Takata, K., Ogochi, K., Watanabe, S., and Kawamiya, M.: Development of the MIROC-ES2L Earth system model and the evaluation of biogeochemical processes and feedbacks, Geosci. Model Dev., 13, 2197–2244, https://doi.org/10.5194/gmd-13-2197-2020, 2020.

Heimdal, T. H., McKinley, G. A., Sutton, A. J., Fay, A. R., and Gloege, L.: Assessing improvements in global ocean pCO_2 machine learning reconstructions with Southern Ocean autonomous sampling, Biogeosciences, 21, 2159–2176, https://doi.org/10.5194/bg-21-2159-2024, 2024.

Honkanen, M., Tuovinen, J.-P., Laurila, T., Mäkelä, T., Hatakka, J., Kielosto, S., and Laakso, L.: Measuring turbulent CO_2 fluxes with a closed-path gas analyzer in a marine environment, Atmos. Meas. Tech., 11, 5335–5350, https://doi.org/10.5194/amt-11-5335-2018, 2018.

867 Hurrell, J. W., Holland, M. M., Gent, P. R., Ghan, S., Kay, J. E., Kushner,
868 P. J., Lamarque, J.-F., Large, W. G., Lawrence, D., Lindsay, K.,
869 Lipscomb, W. H., Long, M. C., Mahowald, N., Marsh, D. R., Neale,
870 R. B., Rasch, P., Vavrus, S., Vertenstein, M., Bader, D., Collins, W.
871 D., Hack, J. J., Kiehl, J., and Marshall, S.: The Community Earth
872 System Model: A framework for collaborative research, Bull. Amer.
873 Meteor. Soc., 94, 1339–1360, https://doi.org/10.1175/BAMS-D-12-
874 00121.1, 2013.

875 Jacobson, A. R., Gruber, N., Sarmiento, J. L., Gloor, M. and Fletcher,
876 S. E. M.: A joint atmosphere-ocean inversion for surface fluxes of
877 carbon dioxide: I. methods and global-scale fluxes, Global.
878 Biogeochem. Cy., 21, GB1020,
879 https://doi.org/10.1029/2005GB002556, 2007.

880 Jacobson, A. R., Schuldt, K. N., Tans, P., Arlyn Andrews, Miller, J. B.,
881 Oda, T., Mund, J., Weir, B., Ott, L., Aalto, T., Abshire, J. B., Aikin,
882 K., Aoki, S., Apadula, F., Arnold, S., Baier, B., Bartyzel, J.,
883 Beyersdorf, A., Biermann, T., Biraud, S. C., Boenisch, H.,
884 Brailsford, G., Brand, W. A., Chen, G., Huilin Chen, Lukasz Chmura,
885 Clark, S., Colomb, A., Commane, R., Conil, S., Couret, C., Cox, A.,
886 Cristofanelli, P., Cuevas, E., Curcoll, R., Daube, B., Davis, K. J.,
887 Wekker, S. de, Della Coletta, J., Delmotte, M., DiGangi, E., DiGangi,
888 J. P., Di Sarra, A. G., Dlugokencky, E., Elkins, J. W., Emmenegger,
889 L., Shuangxi Fang, Fischer, M. L., Forster, G., Frumau, A.,
890 Galkowski, M., Gatti, L. V., Gehrlein, T., Gerbig, C., Francois
891 Gheusi, Gloor, E., Gomez-Trueba, V., Goto, D., Griffis, T., Hammer,
892 S., Hanson, C., Haszpra, L., Hatakka, J., Heimann, M., Heliasz, M.,
893 Hensen, A., Hermansen, O., Hintsa, E., Holst, J., Ivakhov, V., Jaffe,
894 D. A., Jordan, A., Joubert, W., Karion, A., Kawa, S. R., Kazan, V.,
895 Keeling, R. F., Keronen, P., Kneuer, T., Kolari, P., Kateřina
896 Komínková, Kort, E., Kozlova, E., Krummel, P., Kubistin, D.,
897 Labuschagne, C., Lam, D. H., Lan, X., Langenfelds, R. L., Laurent,
898 O., Laurila, T., Lauvaux, T., Lavric, J., Law, B. E., Lee, J., Lee, O.
899 S., Lehner, I., Lehtinen, K., Leppert, R., Leskinen, A., Leuenberger,
900 M., Levin, I., Levula, J., Lin, J., Lindauer, M., Loh, Z., Lopez, M.,
901 Luijkx, I. T., Lunder, C. R., Machida, T., Mammarella, I., Manca,
902 G., Manning, A., Manning, A., Marek, M. V., Martin, M. Y.,
903 Matsueda, H., McKain, K., Meijer, H., Meinhardt, F., Merchant, L.,
904 N. Mihalopoulos, Miles, N. L., Miller, C. E., Mitchell, L., Mölder,
905 M., Montzka, S., Moore, F., Moossen, H., Morgan, E., Josep-Anton
906 Morgui, Morimoto, S., Müller-Williams, J., J. William Munger,
907 Munro, D., Myhre, C. L., Shin-Ichiro Nakaoka, Jaroslaw Necki,
908 Newman, S., Nichol, S., Niwa, Y., Obersteiner, F., O'Doherty, S.,
909 Paplawsky, B., Peischl, J., Peltola, O., Piacentino, S., Jean-Marc
910 Pichon, Pickers, P., Piper, S., Pitt, J., Plass-Dülmer, C., Platt, S. M.,
911 Prinzivalli, S., Ramonet, M., Ramos, R., Reyes-Sanchez, E.,
912 Richardson, S. J., Riris, H., Rivas, P. P., Ryerson, T., Saito, K.,
913 Sargent, M., Sasakawa, M., Scheeren, B., Schuck, T., Schumacher,
914 M., Seifert, T., Sha, M. K., Shepson, P., Shook, M., Sloop, C. D.,
915 Smith, P., Stanley, K., Steinbacher, M., Stephens, B., Sweeney, C.,

Thoning, K., Timas, H., Torn, M., Tørseth, K., Trisolino, P., Turnbull, J., van den Bulk, P., van Dinther, D., Vermeulen, A., Viner, B., Vitkova, G., Walker, S., Watson, A., Wofsy, S. C., Worsey, J., Worthy, D., Dickon Young, Zaehle, S., Zahn, A., and Zimnoch, M.: CarbonTracker CT2022, Model published by NOAA Global Monitoring Laboratory, https://doi.org/10.25925/z1gj-3254 (last access: 20 May 2026), 2023.

Jin, C. X., Zhou, T. J., Chen, X. L., and Wu, B: Seasonally evolving dominant interannual variability mode of air–sea CO_2 flux over the western North Pacific simulated by CESM1-BGC, Sci. China Earth Sci. 60, 1854–1865, https://doi.org/10.1007/s11430-015-9085-4, 2017.

Johansson, M. M., Björkqvist, J.-V., Särkkä, J., Leijala, U., and Kahma, K. K.: Correlation of wind waves and sea level variations on the coast of the seasonally ice-covered Gulf of Finland, Nat. Hazards Earth Syst. Sci., 22, 813–829, https://doi.org/10.5194/nhess-22-813-2022, 2022.

Koseki, S., Tjiputra, J., Fransner, F., Crespo, L. R., and Keenlyside, N. S.: isentangling the impact of Atlantic Niño on sea–air CO_2 flux. Nat. Commun. 14, 3649, https://doi.org/10.1038/s41467-023-38718-9, 2023.

Krall, K. E., Smith, A. W., Takagaki, N., and Jähne, B.: Air–sea gas exchange at wind speeds up to 85 m s^{-1}, Ocean Sci., 15, 1783–1799, https://doi.org/10.5194/os-15-1783-2019, 2019.

Lan, Y.-Y., Hsu, H.-H., Tsuang, B.-J., and Tu, C.-Y.: rceclccr/CAM5_SIT_v1.0 (v1.0.0), Zenodo [code], https://doi.org/10.5281/zenodo.5510795, 2021.

Lan, Y.-Y.: POP2-waves coupled model in CESM1.2.2 framework, Zenodo [code], https://doi.org/10.5281/zenodo.15795234, 2025.

Li, S, Babanin, A. V., and Guan, C.: Dimensionless Parameterizations of Air–Sea CO_2 Gas Transfer Velocity on Surface Waves, Tellus B: Chem. Phys. Meteorol., 75(1), 1–12, https://doi.org/10.16993/tellusb.1867, 2023.

Liu, B., Six, K. D., and Ilyina, T.: Incorporating the stable carbon isotope 13C in the ocean biogeochemical component of the Max Planck Institute Earth System Model, Biogeosciences, 18, 4389–4429, https://doi.org/10.5194/bg-18-4389-2021, 2021.

Long, M. C., Lindsay, K., Peacock, S., Moore, J. K., and Doney, S. C.: Twentieth-Century oceanic carbon uptake and storage in CESM1 (BGC), J. Climate, 26, 6775–6800, https://doi.org/10.1175/JCLI-D-12-00184.1, 2013.

Long, M. C., Moore, J. K., Lindsay, K., Levy, M., Doney, S. C., Luo, J. Krumhardt, K. M., Letscher, R. T., Grover, M., and Sylvester, T.: Simulations with the marine biogeochemistry library (MARBL). J.

Adv. Model. Earth Sy., 13(12), e2021MS002647. https://doi.org/10.1029/2021MS002647, 2021.

Lovato, T., Peano, D., Butenschön, M., Materia, S., Iovino, D., Scoccimarro, E., Fogli, P. G., Cherchi, A., Bellucci, A., Gualdi, S., Masina, S., and Navarra, A.: CMIP6 Simulations With the CMCC Earth System Model (CMCC-ESM2), J. Adv. Model. Earth Sy., 14, e2021MS002814, https://doi.org/10.1029/2021MS002814, 2022.

Lovenduski, N. S., Yeager, S. G., Lindsay, K., and Long, M. C.: Predicting near-term variability in ocean carbon uptake, Earth Syst. Dynam., 10, 45–57, https://doi.org/10.5194/esd-10-45-2019, 2019.

Macovei, V. A., Petersen, W., Brix, H., and Voynova, Y. G.: Reduced ocean carbon sink in the south and central North Sea (2014–2018) revealed from FerryBox observations Geophys. Res. Lett., 48, e2021GL092645, https://doi.org/10.1029/2021GL092645, 2021.

Mauritsen, T., Bader, J., Becker, T., Behrens, J., Bittner, M., Brokopf, R., Brovkin, V., Claussen, M., Crueger, T., Esch, M., Fast, I., Fiedler, S., Flaeschner, D., Gayler, V., Giorgetta, M., Goll, D. S., Haak, H., Hagemann, S., Hedemann, C., Hohenegger, C., Ilyina, T., Jahns, T., Jimenéz-de-la Cuesta, D., Jungclaus, J., Kleinen, T., Kloster, S., Kracher, D., Kinne, S., Kleberg, D., Lasslop, G., Kornblueh, L., Marotzke, J., Matei, D., Meraner, K., Mikolajewicz, U., Modali, K., Moebis, B., Mueller, W. A., Nabel, J. E. M. S., Nam, C. C. W., Notz, D., Nyawira, S.-S., Paulsen, H., Peters, K., Pincus, R., Pohlmann, H., Pongratz, J., Popp, M., Raddatz, T. J., Rast, S., Redler, R., Reick, C. H., Rohrschneider, T., Schemann, V., Schmidt, H., Schnur, R., Schulzweida, U., Six, K. D., Stein, L., Stemmler, I., Stevens, B., von Storch, J.-S., Tian, F., Voigt, A., Vrese, P., Wieners, K.-H., Wilkenskjeld, S., Winkler, A., and Roeckner, E.: Developments in the MPI-M Earth System Model version 1.2 (MPI-ESM1.2) and Its Response to Increasing CO_2, J. Adv. Model. Earth Sy., 11, 998–1038, https://doi.org/10.1029/2018MS001400, 2019.

McKinley, G. A., Fay, A. R., Eddebbar, Y. A., Gloege, L., and Lovenduski, N. S.: External forcing explains recentdecadal variability of the ocean carbonsink, AGU Advances, 1,e2019AV00014, https://doi.org/10.1029/2019AV000149, 2020.

Mellor, G. L., Donelan, M. A., and Oey, L.-Y.: A surface wave model for coupling with numerical ocean circulation models. J. Atmos. Ocean. Technol., 25(10), 1785–1807, https://doi.org/10.1175/2008JTECHO573.1, 2008.

Monahan, E. C., and Spillane, M. C.: The role of oceanic whitecaps in air–sea gas exchange, in: Gas transfer at water surfaces, edited by: Brutsaert, W. and Jirka, G. H., Reidel, Hingham, MA, 495–503, https://doi.org/10.1007/978-94-017-1660-4_45, 1984.

Moore, J. K., Lindsay, K., Doney, S. C., Long, M. C., and Misumi, K.: Marine ecosystem dynamics and biogeochemical cycling in the

Community Earth System Model [CESM1 (BGC)]: Comparison of the 1990s with the 2090s under the RCP4. 5 and RCP8. 5 scenarios, J. Climate, 26, 9291–9312, https://doi.org/10.1175/JCLI-D-12-00566.1, 2013.

Müller, J. D., Gruber, N., Carter, B., Feely, R., Ishii, M., Lange, N., Lauvset, S. K., Murata, A., Olsen, A., Pérez, F. F., Sabine, C., Tanhua, T., Wanninkhof, R., and Zhu, D.: Decadal trends in the oceanic storage of anthropogenic carbon from 1994 to 2014. AGU Advances, 4, e2023AV000875, https://doi.org/10.1029/2023AV000875, 2023.

Reichl, B. G., and Deike, L.: Contribution of Sea-State Dependent Bubbles to Air–sea Carbon Dioxide Fluxes, Geophys. Res. Lett., 47, e2020GL087267. https://doi.org/10.1029/2020GL087267, 2020.

Roobaert, A., Resplandy, L., Laruelle, G. G., Liao, E., and Regnier, P.: Unraveling the physical and biological controls of the global coastal CO_2 sink, Global Biogeochem. Cy., 38, e2023GB007799. https://doi.org/10.1029/2023GB007799, 2024.

Rustogi, P., Resplandy, L., Liao, E., Reichl, B. G., and Deike, L.: Influence of wave-induced variability on ocean carbon uptake. Global Biogeochem. Cy., 39, e2024GB008382. https://doi.org/10.1029/2024GB008382, 2025.

Sabine, C., Sutton, A., McCabe, K., Lawrence-Slavas, N., Alin, S, Feely, R., Jenkins, R., Maenner, S., Meinig, C., Thomas, J., van Ooijen, E., Passmore, A., and Tilbrook, B.: Evaluation of a new carbon dioxide system for autonomous surface vehicles, J. Atmos. Oceaen. Tech., 37, 1305–1317, https://doi.org/10.1175/JTECH-D-20-0010.1, 2020.

Séférian, R., Nabat, P., Michou, M., Saint-Martin, D., Voldoire, A., Colin, J., Decharme, B., Delire, C., Berthet, S., Chevallier, M., Sénési, S., Franchisteguy, L., Vial, J., Mallet, M., Joetzjer, E., Geoffroy, O., Guérémy, J.-F., Moine, M.-P., Msadek, R., Ribes, A., Rocher, M., Roehrig, R., Salas-y-Mélia, D., Sanchez, E., Terray, L., Valcke, S., Waldman, R., Aumont, O., Bopp, L., Deshayes, J., Éthé, C., and Madec, G.: Evaluation of CNRM Earth-System model, CNRM-ESM2-1: role of Earth system processes in present-day and future climate, J. Adv. Model. Earth Sy., 11, 4182–4227, https://doi.org/10.1029/2019MS001791, 2019.

Seland, Ø., Bentsen, M., Olivié, D., Toniazzo, T., Gjermundsen, A., Graff, L. S., Debernard, J. B., Gupta, A. K., He, Y.-C., Kirkevåg, A., Schwinger, J., Tjiputra, J., Aas, K. S., Bethke, I., Fan, Y., Griesfeller, J., Grini, A., Guo, C., Ilicak, M., Karset, I. H. H., Landgren, O., Liakka, J., Moseid, K. O., Nummelin, A., Spensberger, C., Tang, H., Zhang, Z., Heinze, C., Iversen, T., and Schulz, M.: Overview of the Norwegian Earth System Model (NorESM2) and key climate response of CMIP6 DECK, historical, and scenario simulations, Geosci. Model Dev., 13, 6165–6200,

https://doi.org/10.5194/gmd-13-6165-2020, 2020.

Shutler, J. D., Wanninkhof, R., Nightingale, P. D., Woolf, D. K., Bakker, D. C., Watson, A., Ashton, I., Holding, T., Chapron, B., Quilfen, Y., Fairall, C., Schuster, U., Nakajima, M., and Donlon, C. J.: Satellites will address critical science priorities for quantifying ocean carbon, Front. Ecol. Environ., 18(1): 27–35, http://dx.doi.org/10.1002/fee.2129, 2019.

Sigmond, M., Anstey, J., Arora, V., Digby, R., Gillett, N., Kharin, V., Merryfield, W., Reader, C., Scinocca, J., Swart, N., Virgin, J., Abraham, C., Cole, J., Lambert, N., Lee, W.-S., Liang, Y., Malinina, E., Rieger, L., von Salzen, K., Seiler, C., Seinen, C., Shao, A., Sospedra-Alfonso, R., Wang, L., and Yang, D.: Improvements in the Canadian Earth System Model (CanESM) through systematic model analysis: CanESM5.0 and CanESM5.1, Geosci. Model Dev., 16, 6553–6591, https://doi.org/10.5194/gmd-16-6553-2023, 2023.

Signorini, S. R., and McClain, C. R.: Effect of uncertainties in climatologic wind, ocean pCO_2, and gas transfer algorithms on the estimate of global sea–air CO_2 flux, Global Biogeochem. Cy., 23, GB2025, https://doi.org/10.1029/2008GB003246, 2009.

Smith, R., Jones, P., Briegleb, B., Bryan, F., Danabasoglu, G., Dennis, J., Dukowicz, J., Eden, C., Fox-Kemper, B., Gent, P., Hecht, M., Jayne, S., Jochum, M., Large, W., Lindsay, K., Maltrud, M., Norton, N., Peacock, S., Vertenstein, M., and Yeager, S.: The Parallel Ocean Program (POP) reference manual ocean component of the Community Climate System Model (CCSM) and Community Earth System Model (CESM), Los Alamos National Laboratory Tech. Rep. LAUR-10-01853, 140 pp, https://www2.cesm.ucar.edu/models/cesm1.0/pop2/doc/sci/POPRefManual.pdf, 2010.

Soloviev, A., and Lukas, R.: Effects of Bubbles and Sea Spray on Air–Sea Exchange in Hurricane Conditions, Bound.-Layer Meteorol., 136, 365–376, https://doi.org/10.1007/s10546-010-9505-0, 2010.

Stock, C. A., Dunne, J. P., Fan, S., Ginoux, P., John, J., Krasting, J. P., Laufkötter, C., Paulot, F., and Zadeh, N.: Ocean biogeochemistry in GFDL's Earth System Model 4.1 and its response to increasing atmospheric CO_2, J. Adv. Model. Earth Sy., 12, e2019MS002043, https://doi.org/10.1029/2019MS002043, 2020.

Sutton, A. J., Sabine, C. L., Maenner-Jones, S., Lawrence-Slavas, N., Meinig, C., Feely, R. A., Mathis, J. T., Musielewicz, S., Bott, R., McLain, P. D., Fought, H. J., and Kozyr, A.: A high-frequency atmospheric and seawater pCO_2 data set from 14 open-ocean sites using a moored autonomous system, Earth Syst. Sci. Data, 6, 353–366, https://doi.org/10.5194/essd-6-353-2014, 2014.

Tjiputra, J. F., Schwinger, J., Bentsen, M., Morée, A. L., Gao, S., Bethke, I., Heinze, C., Goris, N., Gupta, A., He, Y.-C., Olivié, D., Seland,

Ø., and Schulz, M.: Ocean biogeochemistry in the Norwegian Earth System Model version 2 (NorESM2), Geosci. Model Dev., 13, 2393–2431, https://doi.org/10.5194/gmd-13-2393-2020, 2020.

Tokoro, T., Hosokawa, S., Miyoshi, E., Tada, K., Watanabe, K., Montani, S., Kayanne, H., and Kuwae, T.: Net uptake of atmospheric CO_2 by coastal submerged aquatic vegetation, Glob. Change Biol., 20, 1873–1884, https://doi.org/10.1111/gcb.12543, 2014.

Van Dam, B., Polsenaere, P., Barreras-Apodaca, A., Lopes, C., Sanchez-Mejia, Z., Tokoro, T., Kuwae, T., Loza, L. G., Rutgersson, A., Fourqurean, J., and Thomas, H.: Global trends in air-water CO_2 exchange over seagrass meadows revealed by atmospheric Eddy Covariance, Global Biogeochem. Cy., 35, e2020GB006848, https://doi.org/10.1029/2020GB006848, 2021.

Wanninkhof, R.: Relationship between wind speed and gas exchange over the ocean, J. Geophys. Res., 97(C5), 7373–7382. https://doi.org/10.1029/92JC00188, 1992.

Wanninkhof, R.: Relationship between wind speed and gas exchange over the ocean revisited, Limnol. Oceanogr.: Methods, 12(6), 351–362. https://doi.org/10.4319/lom.2014.12.351, 2014.

Weiss, R. F.: Carbon dioxide in water and seawater: the solubility of a non-ideal gas, Mar. Chem., 2 (3), pp. 203-215, https://doi.org/10.1016/0304-4203(74)90015-2, 1974.

Williams, N. L., Juranek, L. W., Feely, R. A., Johnson, K. S., Sarmiento, J. L., Talley, L. D., Dickson, A. G., Gray, A. R., Wanninkhof, R., Russell, J. L., and Riser, S. C.: Calculating surface ocean pCO_2 from biogeochemical Argo floats equipped with pH: An uncertainty analysis, Global Biogeochem. Cy., 31, 591–604, https://doi.org/10.1002/2016GB005541, 2017.

Wu, Y., and Qi, D.: The controversial Southern Ocean air–sea CO_2 flux in the era of autonomous ocean observations, Sci. Bull., 68, 21, 2519-2522, https://doi.org/10.1016/j.scib.2023.08.059, 2023.

Wu, L., Cai, Y., and Rutgersson, A.: Ocean surface waves impact on global air-sea CO_2 flux, Biogeochem., 168, 68, https://doi.org/10.1007/s10533-025-01267-y, 2025.

Yang, X., Wynn-Edwards, C. A., Strutton, P. G., and Shadwick, E. H.: Drivers of air–sea CO_2 flux in the subantarctic zone revealed by time series observations. Global Biogeochem. Cy., 38, e2023GB007766, https://doi.org/10.1029/2023GB007766, 2024.

Yool, A., Palmiéri, J., Jones, C. G., de Mora, L., Kuhlbrodt, T., Popova, E. E., Nurser, A. J. G., Hirschi, J., Blaker, A. T., Coward, A. C., Blockley, E. W., and Sellar, A. A.: Evaluating the physical and biogeochemical state of the global ocean component of UKESM1 in CMIP6 historical simulations, Geosci. Model Dev., 14, 3437–3472, https://doi.org/10.5194/gmd-14-3437-2021, 2021.

Zhou, X., Reichl, B. G., Romero, L., and Deike, L.: A sea state dependent gas transfer velocity for CO_2 unifying theory, model, and field data, Earth Space Sci., 10, e2023EA003237, https://doi.org/10.1029/2023EA003237, 2023.

Ziehn, T., Chamberlain, M., Law, R., Lenton, A., Bodman, R., Dix, M., Stevens, L., Wang, Y.-P., and Srbinovsky, J.: The Australian Earth System Model: ACCESS-ESM1.5, J. South. Hemisph. Earth Syst. Sci., 70(1) 193-214, https://doi.org/10.1071/ES19035, 2020.

Table 1. Intercomparison of Earth System Model for estimating air–sea CO_2 flux

Earth System Model	Ocean components	air–sea CO_2 flux consider waves	$K_{w,660}$'s element	Reference
CESM1[1]	POP2[2]	no	U_{10} (Wannikhof 1992)	Chikamoto and DiNezio, 2021; Chikamoto et al., 2023
CESM2[3]	POP2[2]	no	U_{10} (Wannikhof 2014)	Danabasoglu et al., 2020
NorESM2[4]	BLOM[5]	no	U_{10} (Wannikhof 2014)	Seland et al., 2020; Tjiputra et al., 2020
MPI-ESM1.2[6]	MPIOM 1.6[7]	no	U_{10} (Wannikhof 2014)	Mauritsen et al., 2019; Liu et al., 2021
ACCESS-ESM1.5[8]	MOM5[9]	no	U_{10} (Wannikhof 1992)	Ziehn et al., 2020
CMCC-ESM2[10]	NEMO v3.6[11]	no	U_{10} (Wannikhof 1992)	Lovato et al., 2022
CanESM5[12]	CanNEMO[13]	no	U_{10} (Wannikhof 1992)	Sigmond et al., 2023
GFDL-ESM4.1[14]	MOM6[15]	no	U_{10} (Wannikhof 2014)	Stock et al., 2020; Roobaert et al., 2024
IPSL-CM6A-LR[16]	NEMO-PISCES[17]	no	U_{10} (Wannikhof 1992)	Boucher et al., 2020
MIROC-ES2L[18]	COCO 4.0[19]	no	U_{10} (Wannikhof 1992)	Hajima et al., 2020
UKESM1[20]	NEMO v3.6[11]	no	U_{10} (Wannikhof 1992)	Yool et al., 2021
CNRM-ESM2-1[21]	NEMO-PISCES[17]	no	U_{10} (Wannikhof 1992)	Séférian et al., 2019
-[22]	NEMO-PISCES[17]	Yes	H_s, u* (Deike and Melville, 2018)	Wu et al. (2025)
-[22]	MOM6-COBALTv2[23]	Yes	H_s, u* (Deike and Melville, 2018)	Rustogi et al. (2025)
CESM1-POP2–waves[24]	POP2–wave coupled model	Yes	H_s, u* (Deike and Melville, 2018)	This study

Note:

[1]CESM1: the Community Earth System Model version 1 of the National Center for Atmospheric Research (NCAR);

[2]POP2: the Parallel Ocean Program version 2 of NCAR;

[3]CESM2: CESM version 2;

[4]NorESM2: The Norwegian Earth System Model version 2;

[5]BLOM: Bergen Layered Ocean Model;

[6]MPI-ESM1.2: the Max Planck Institute for Meteorology Earth System Model version 1.2;

[7]MPIOM 1.6: the Max-Planck Institute Ocean Model version 1.6;
[8]ACCESS-ESM1.5: the Australian Community Climate and Earth System Simulator form an Earth System Model version 1.5;
[9]MOM5: the GFDL Modular Ocean Model version 5;
[10]CMCC-ESM2: the Euro-Mediterranean Centre on Climate Change (CMCC) Earth System Model version 2;
[11]NEMO v3.6: Nucleus for European Modelling of the Ocean version 3.6;
[12]CanESM5: the Canadian Earth System Model version 5;
[13]CanNEMO: NEMO version 3.4 modified for CanESM;
[14]GFDL-ESM4.1: the Geophysical Fluid Dynamics Laboratory's Earth System Model 4.1;
[15]MOM6: the GFDL Modular Ocean Model version 6;
[16]IPSL-CM6A-LR :version 6 of the Institut Pierre-Simon Laplace (IPSL) climate model;
[17]NEMO-PISCES: Nucleus for European Modelling of the Ocean, Pelagic Interaction Scheme for Carbon and Ecosystem Studies ocean general circulation and biogeochemistry model;
[18]MIROC-ES2L: the Model for Interdisciplinary Research on Climate, Earth System version 2;
[19]COCO 4.0: CCSR (Center for Climate System Research) Ocean Component Model version 4.0:
[20]UKESM1: the U.K. Earth System Model;
[21]CNRM-ESM2-1: the Earth system (ES) model of second generation developed by the Centre National de Recherches Météorologiques (CNRM);
[22]The simulations were conducted using global ocean-only models rather than full Earth System Models.
[23]MOM6-COBALTv2: Geophysical Fluid Dynamics Laboratory global ocean model (Modular Ocean Model, MOM6) coupled with sea ice and biogeochemistry (Carbon, Ocean Biogeochemistry and Lower Trophics, COBALTv2);
[24]CESM1-POP2–waves: POP2–waves coupled model based on CESM1.

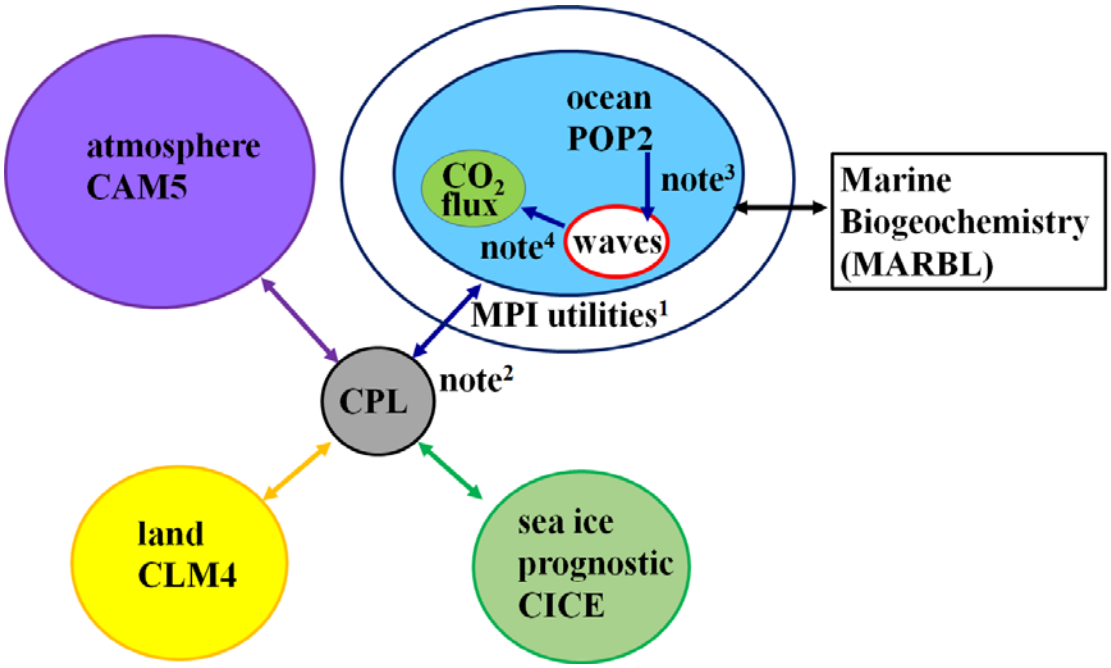

Figure 1. Architecture diagram for POP2–waves experiment in CESM1.2.2 framework, all components adhere to the CESM 1.2.2 framework, except for certain parts of the ocean component. The model components including components for the atmosphere [Community Atmosphere Model version 5 (CAM5)], land [Community Land Model version 4 (CLM4)], ocean [Parallel Ocean Program, version 2 (POP2)], along with its associated modules—the waves module (waves) and the Marine Biogeochemistry (MARBL) module—sea ice [prognostic Los Alamos Sea Ice Model (CICE)], and the coupler (CPL).

Note: [1]The wave-module variables are communicated between neighboring blocks via MPI, including zonal and meridional 10-m winds, wave radiation stress, subsurface momentum, and wave radiation and energy densities.

[2] To transfer variables such as zonal and meridional 10-m winds and friction velocity (including sea surface and ice fraction) from the CPL to POP2.

[3] The wave module receives variables from POP2, including the interpolation of depth-varying currents from z-coordinates (60 levels) to the wave module's vertical sigma coordinates (21 levels), along with ocean grid information in the x, y, and z directions.

[4] The wave module outputs significant wave height and friction velocity from the CPL for calculating the bubble-mediated gas transfer velocity in Eq. (3).

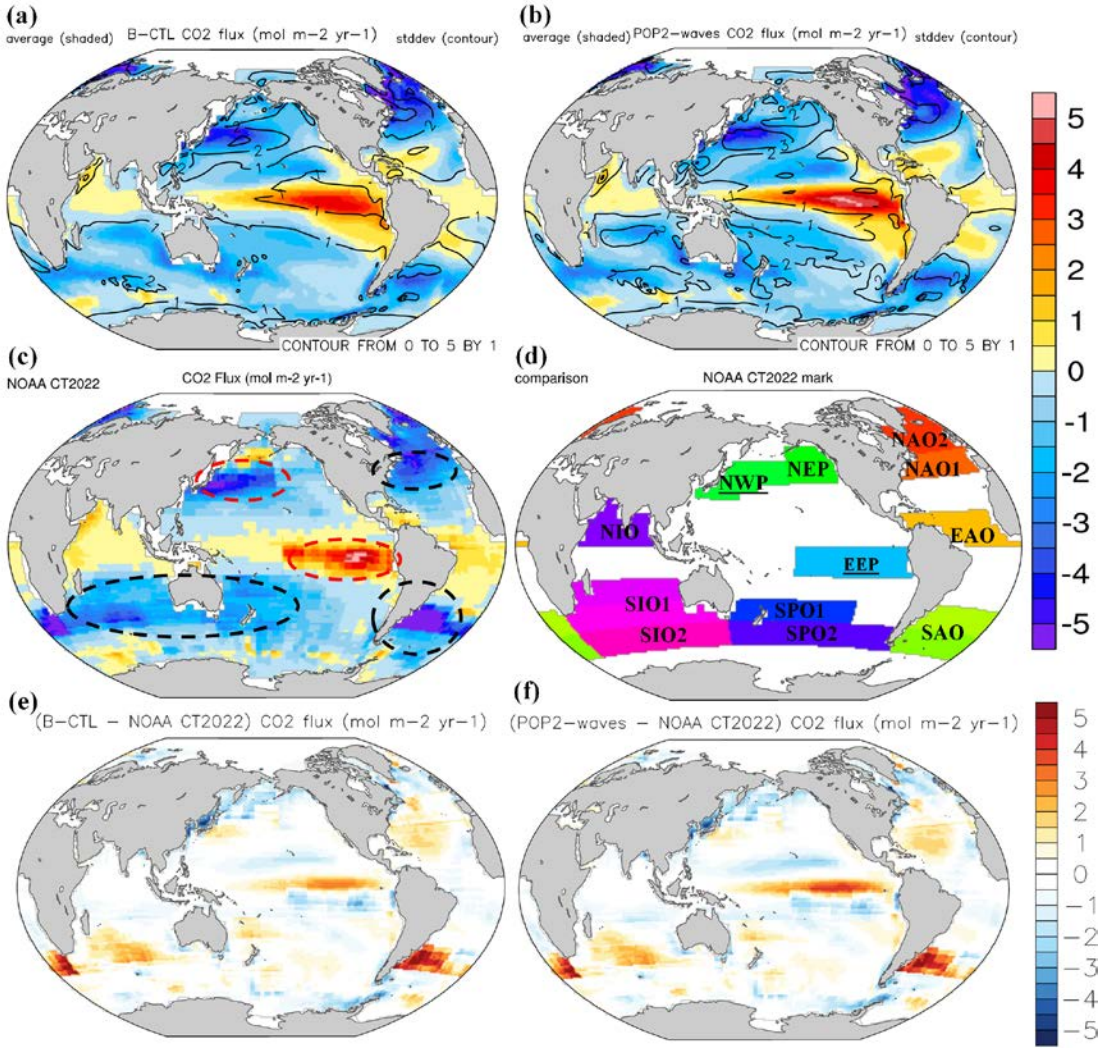

Figure 2. Climatological mean air–sea CO_2 flux (mol m^{-2} yr^{-1}; shaded) and monthly standard deviation (SD: contour): (a) B–CTL; (b) POP2–waves; (c) NOAA CT2022: red dashed lines highlight the positive or negative CO_2 flux in the Pacific, while black dashed lines denote other significant areas; (d) Based on NOAA CT2022, 12 key regions exhibiting significant air–sea CO_2 flux variability have been identified among the 30 ocean basins defined in the CT2022 model documentation (Jacobson et al., 2023) for optimizing flux inversions. These include: (1) Pacific Ocean – Northwestern Pacific (NWP), Eastern Equatorial Pacific (EEP), Northeastern Pacific (NEP), South Pacific Ocean 1 (SPO1), and South Pacific Ocean 2 (SPO2); (2) Indian Ocean – North Indian Ocean (NIO), South Indian Ocean 1 (SIO1), and South Indian Ocean 2 (SIO2); (3) Atlantic Ocean – North Atlantic Ocean 1 (NAO1), North Atlantic Ocean 2 (NAO2), Equatorial Atlantic Ocean (EAO), and South Atlantic Ocean (SAO), (e) the air–sea CO_2 flux difference between B–CTL and NOAA CT2022, and (f) the air–sea CO_2 flux difference between POP2-waves and NOAA CT2022.

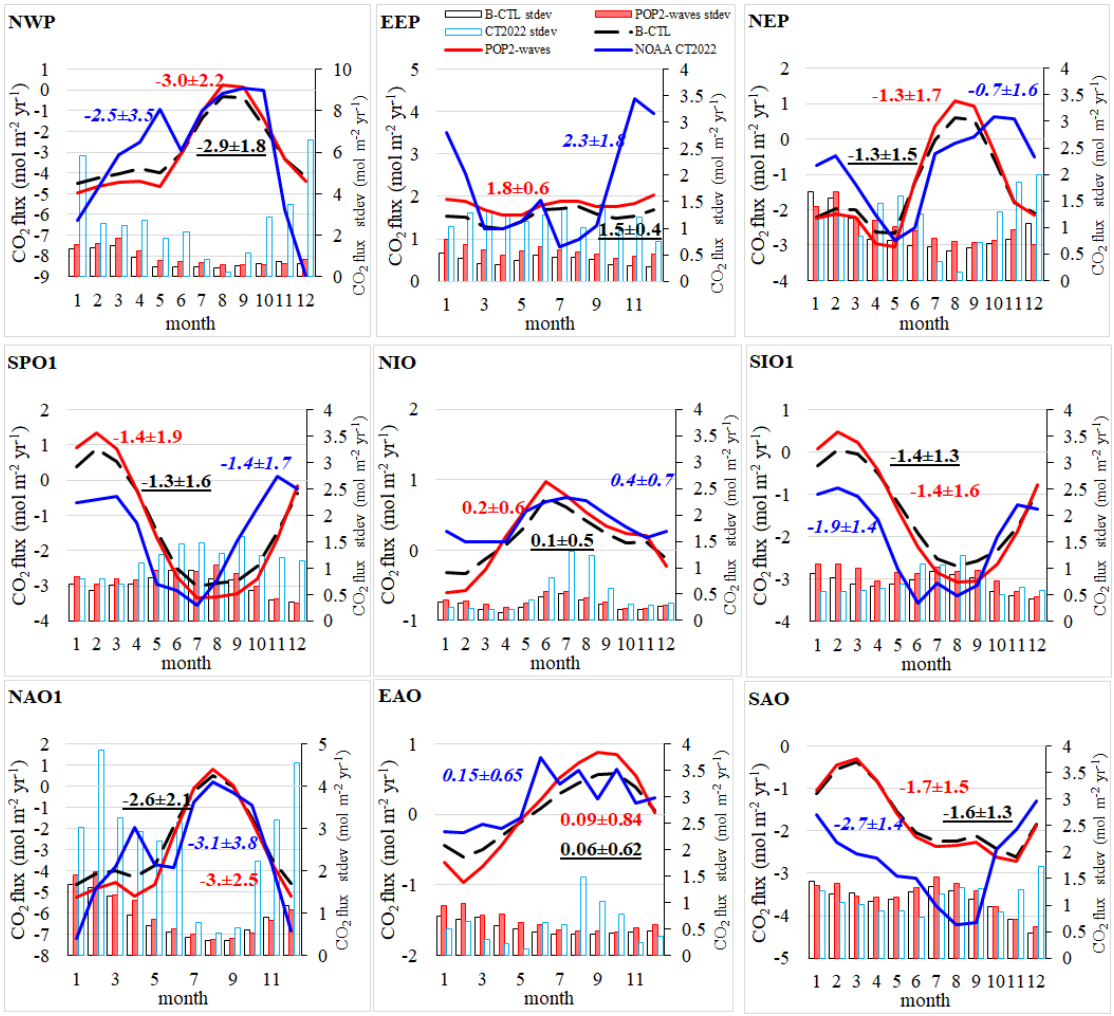

Figure 3. The monthly mean values of the high-correlation climatological average of CO_2 flux with NOAA CT2022 are based on nine characteristic regions (NWP, EEP, NEP, SPO1, NIO, SIO1, NAO1, EAO, and SAO) shown in Fig. 2d. The black dashed line represents B–CTL, the red solid line represents POP2–waves, and the blue solid line represents NOAA CT2022. The bar graph illustrates the standard deviation (stdev) for each month. Black hollow bars correspond to B–CTL, red solid bars to POP2–waves, and light blue hollow bars to NOAA CT2022.

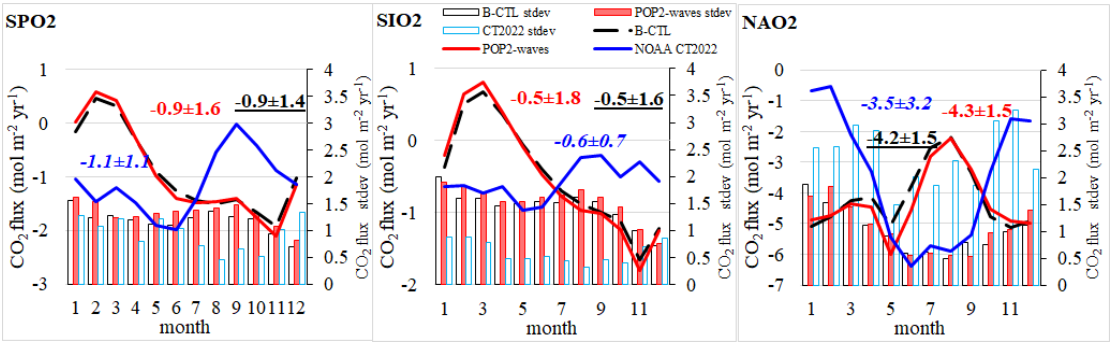

Figure 4. Same as Fig. 3, but for the low-correlation climatological average of the simulated CO_2 flux compared with NOAA CT2022, based on the three characteristic regions (SPO2, SIO2, and NAO2).

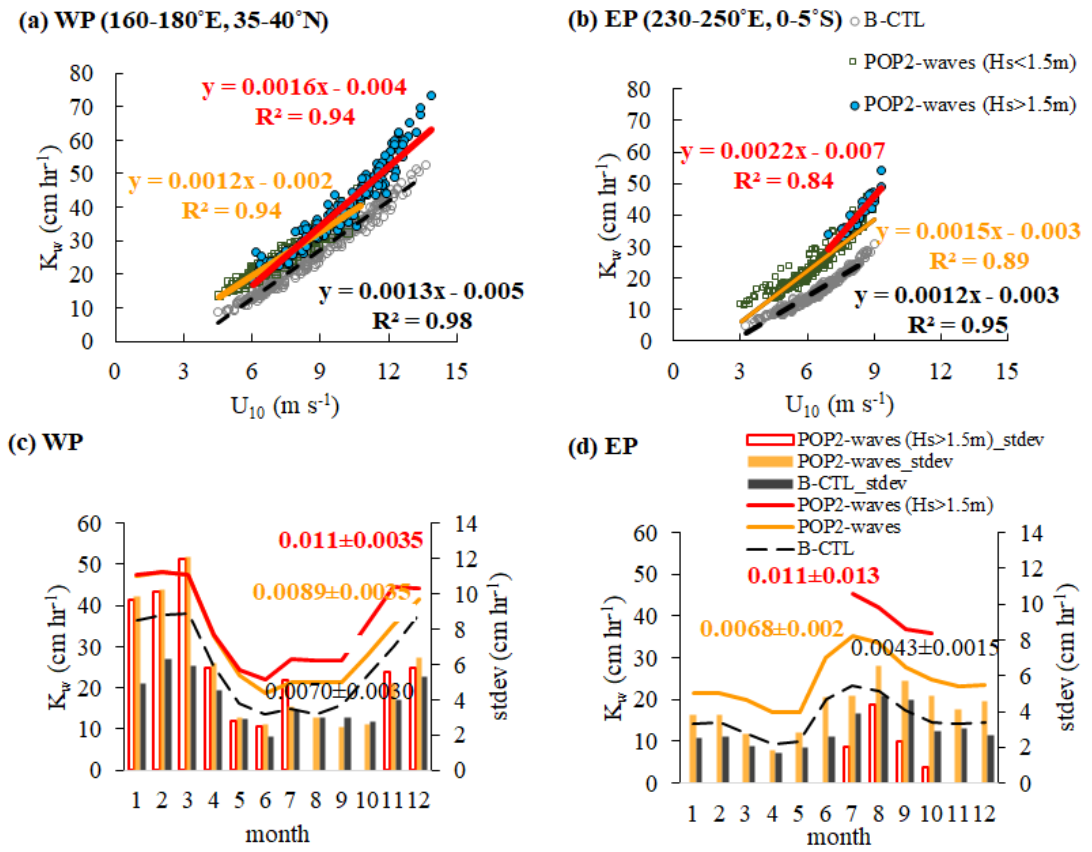

Figure 5. Scatter plots of monthly averaged gas transfer velocity ($K_{w,660}$) versus U_{10} for (a) the Western Pacific (WP; 160–180°E, 35–40°N) and (b) the Eastern Pacific (EP; 230–250°E, 0–5°S). Gray open circles, green open squares, and blue dots with black edges represent B–CTL, POP2–waves data for H_s < 1.5 m, and H_s > 1.5 m, respectively. Corresponding simple linear regressions (SLRs) and squared correlation coefficients (R^2) are shown with black dotted lines/text (B–CTL), orange solid lines/text (POP2–waves, H_s < 1.5 m), and red solid lines/text (POP2–waves, H_s > 1.5 m). Panels (c) and (d) display the monthly mean values of $K_{w,600}$ for WP and EP, respectively. Red and orange solid lines/text indicate POP2–waves (H_s > 1.5 m) and the average of all POP2–waves data, while the black dotted line/text represents B–CTL. The bar graph illustrates the standard deviation (stdev) for each month over the WP and EP, red hollow bars for POP2–waves (H_s > 1.5 m), orange for average POP2–waves, and black for B–CTL.

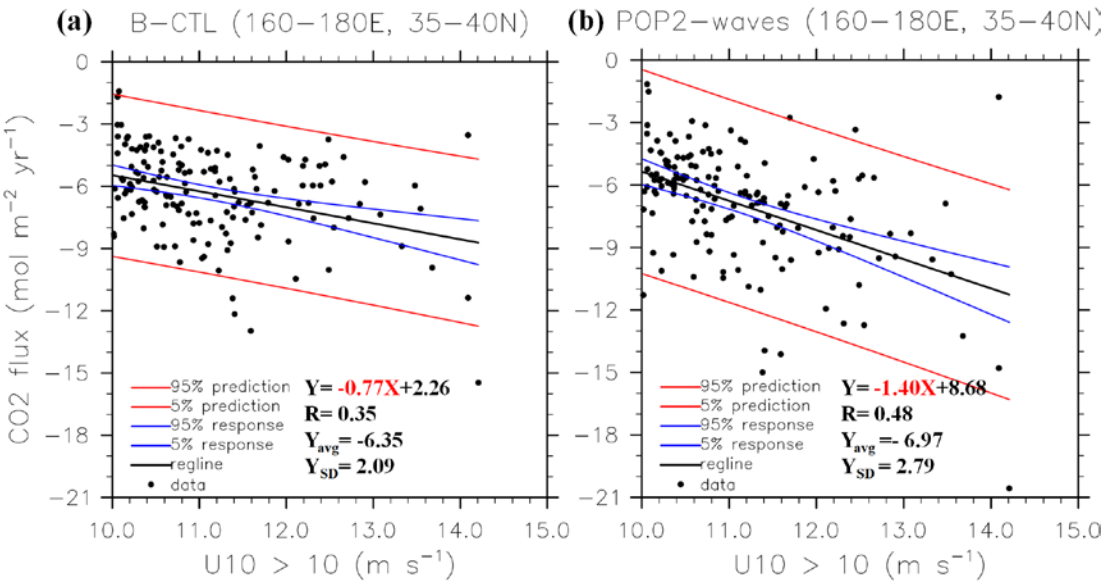

Figure 6. Scatter plots of air–sea CO_2 flux versus U_{10} with regression lines over the Western Pacific (160–180°E, 35–40°N) under high-wind conditions (U_{10} > 10 m s^{-1}) for (a) B–CTL and (b) POP2–waves experiments. Black dots indicate monthly mean values from each experiment. Blue lines denote the 95% and 5% confidence limits of the mean response, while red lines denote the 95% and 5% prediction intervals. The regression equation (Y = mx + b), correlation coefficient (R), mean CO_2 flux (Y_{avg}), and standard deviation (Y_{SD}) are shown to the right of the legend.

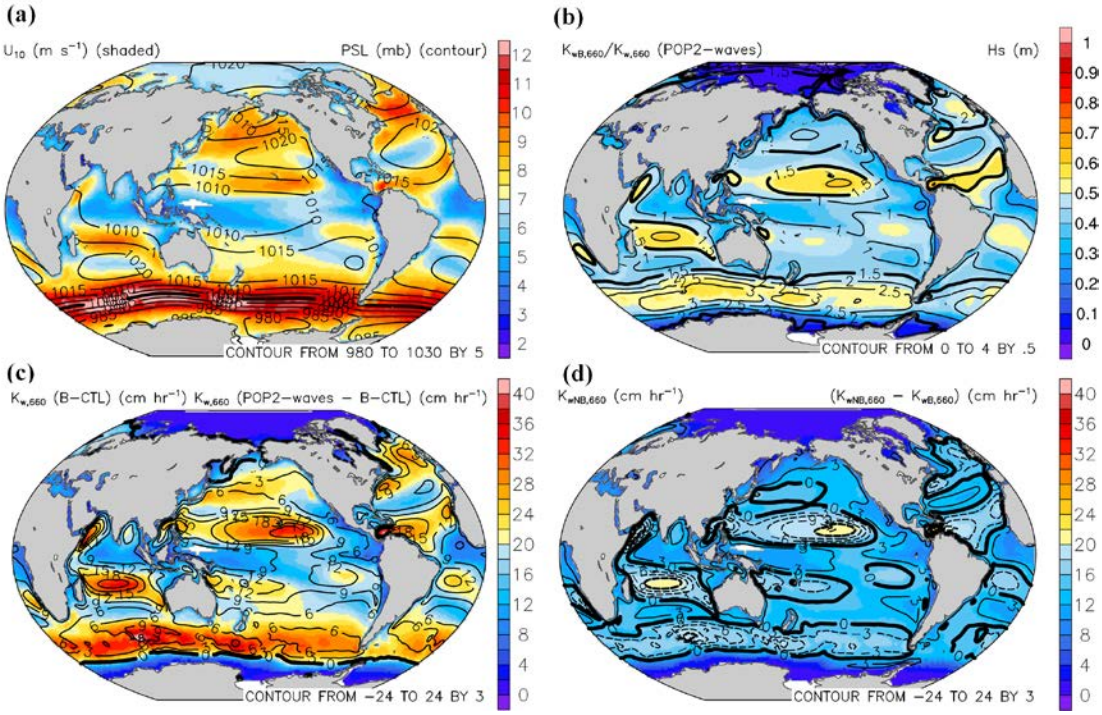

Figure 7. The average gas transfer velocity is influenced by the atmospheric factor and its corresponding ratio, as depicted in the figure: (a) Shaded areas represent 10-m wind speed (U_{10}, m s^{-1}), with contours indicating sea level pressure (PSL, mb). (b) The ratio of bubble-mediated components ($K_{wB,660}$) to POP2–waves $K_{w,660}$ is shown in color, with contours representing significant wave height H_s (m). (c) Shaded areas represent $K_{w,660}$ (B–CTL), with contours depicting the difference $K_{w,660}$ (POP2–waves − B–CTL) in cm hr^{-1}. (d) Shaded areas show the non-bubble-mediated component ($K_{wNB,660}$), while contours represent the difference ($K_{wNB,660} - K_{wB,660}$) in cm hr^{-1}.

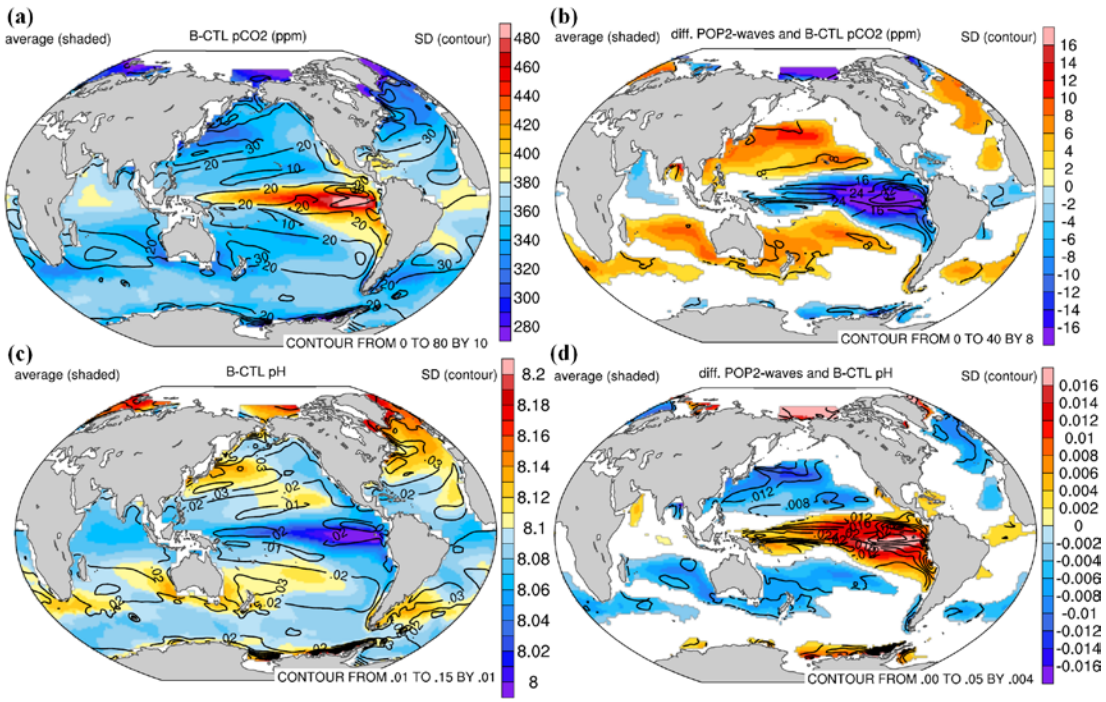

Figure 8. The 30-year average and model difference of pCO_2^w (ppm; panels a and b) and ocean surface pH (panels c and d), with the average represented by shading and the standard deviation by contours. Panels (a) and (c) present results from the B–CTL experiment, while panels (b) and (d) depict the differences between the POP2–waves and B–CTL experiments with a T-score corresponding to a 95% confidence level.

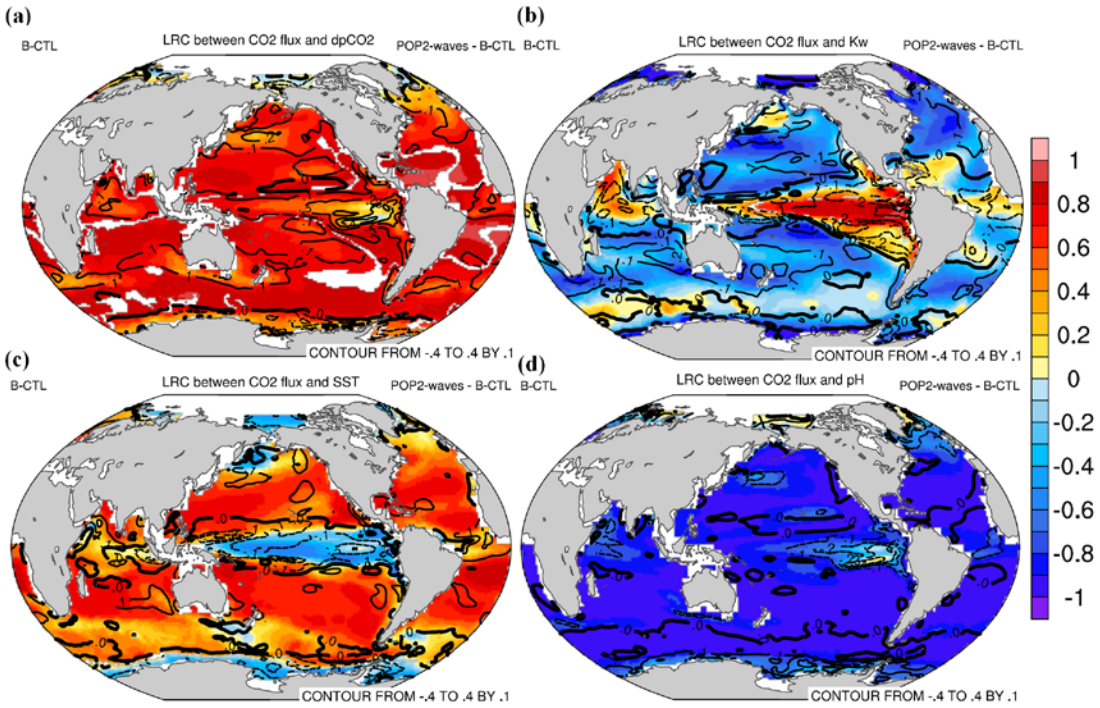

Figure 9. The 30-year averages of the linear regression coefficients (LRC) between CO_2 flux and (a) $dpCO_2$, (b) $K_{w,660}$, (c) SST, and (d) pH are shown for B–CTL (shaded), with contours representing differences between POP2–waves and B–CTL. White areas indicate LRCs that are insignificant at the 95% confidence level. All variables were normalized before regression.

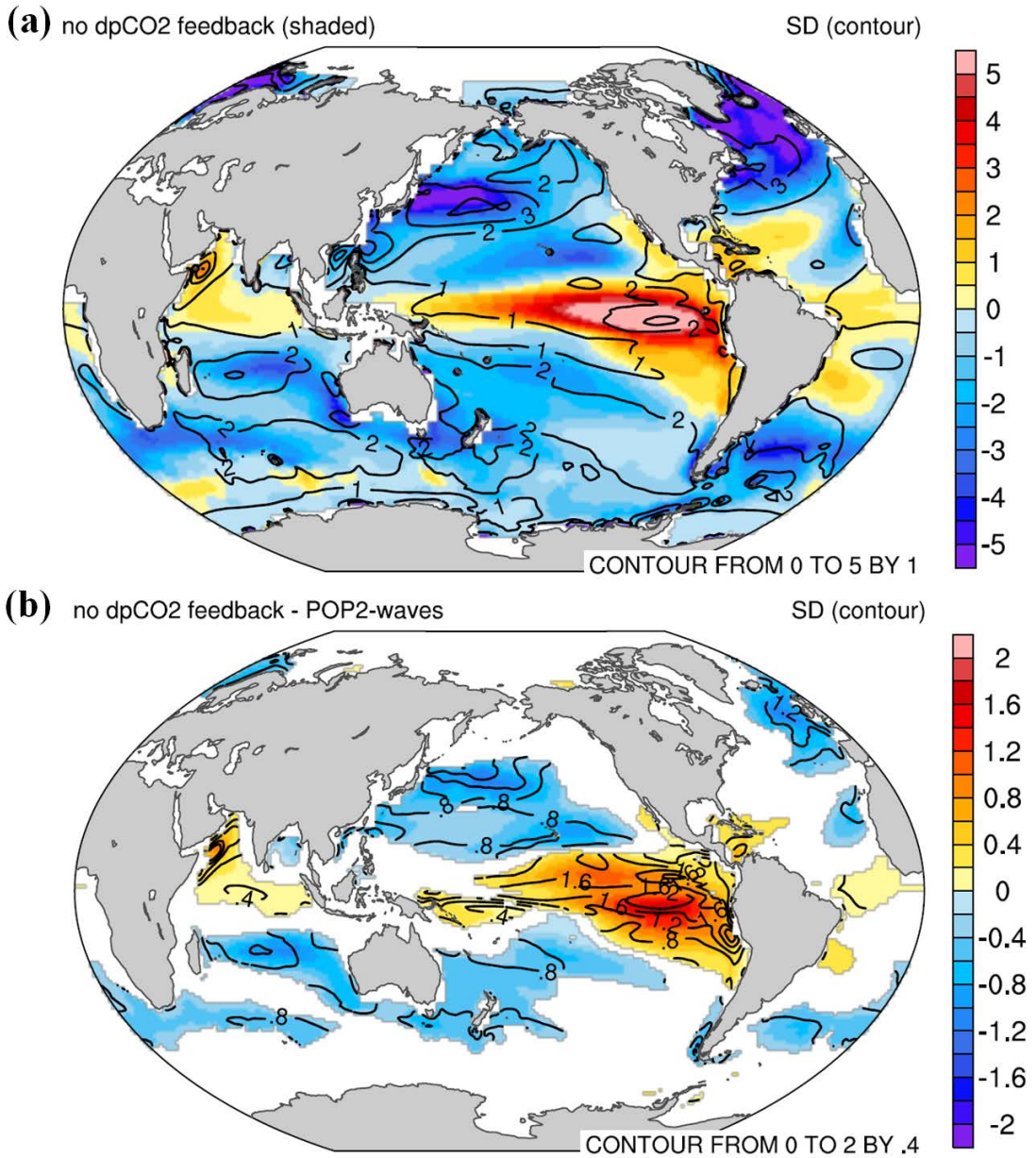

Figure 10. Estimated air–sea CO_2 flux assuming lack of $dpCO_2$-driven negative feedback. (a) CO_2 flux calculated using independent $dpCO_2$ values (from B–CTL) and $K_{w,660}$ incorporating wave effects (labeled as "lack of $dpCO_2$-driven negative feedback"), with shading representing the mean and contours indicating the SD, (b) Difference in CO_2 flux between the "lack of $dpCO_2$-driven negative feedback" case and the POP2–waves simulation, with shading for the mean difference and contours for the SD passing a 95% confidence level.

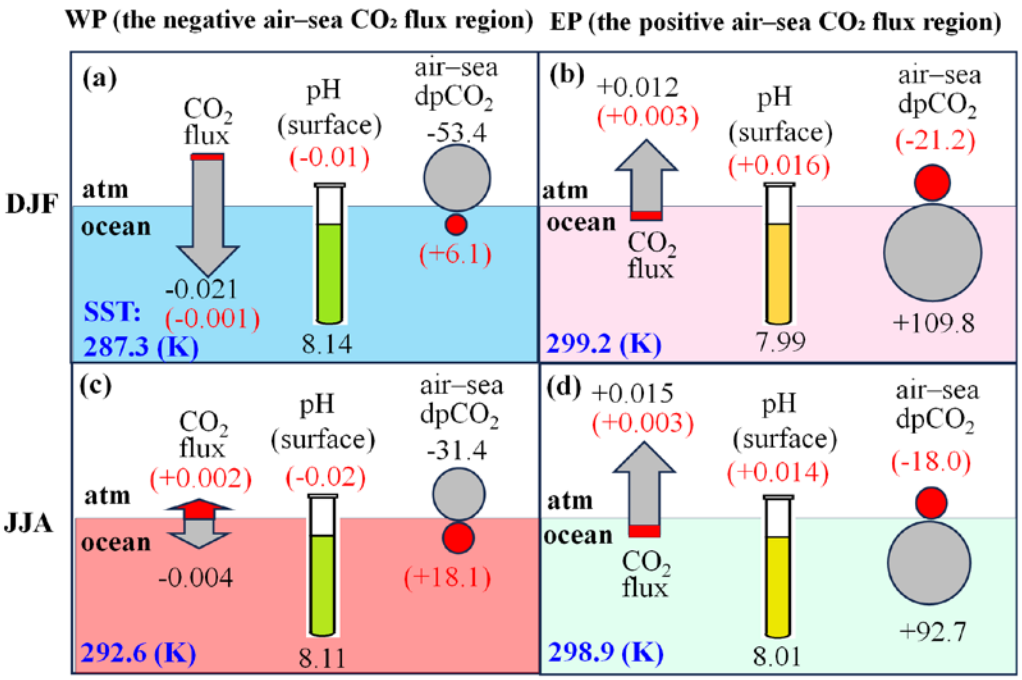

Figure 11. Schematic diagrams illustrate B–CTL (gray colors) and the differences between POP2–waves and B–CTL (red colors) in air–sea CO_2 flux (arrows), surface pH (tube colors indicator), and air–sea $dpCO_2$ (circle markers) over the negative air–sea CO_2 flux region (WP; 160–180°E, 35–40°N) and the positive air–sea CO_2 flux region (EP; 230–250°E, 0–5°S). Each panel includes an ocean-atmosphere interface, with ocean color shading representing relative SST levels across different seasons. The lower-left corner displays the SST value, (a) WP in DJF seasonal mean, (b) EP in DJF seasonal mean, (c) WP in JJA seasonal mean, and (d) EP in JJA seasonal mean.